Modeling urban traffic heat flux in the Community Earth System Model: Formulation and validation for two sites

Yuan Sun[1], Keith W. Oleson[2], Zhonghua Zheng[1]

[1]Department of Earth and Environmental Sciences, The University of Manchester, Manchester M13 9PL, UK
[2]Climate and Global Dynamics Laboratory, NSF National Center for Atmospheric Research, Boulder, CO 80307, USA

Key Points:

- We developed an urban traffic module in CESM to model traffic heat flux in a bottom-up way.
- Online traffic heat modeling improves the simulation of anthropogenic heat flux, which by default only accounts for building energy use.
- Traffic heat increased the simulated annual mean air temperature by 0.4 K and 0.25 K at FR-Capitole and UK-Manchester sites, respectively.

Corresponding author: Yuan Sun, yuan.sun@manchester.ac.uk

Corresponding author: Zhonghua Zheng, zhonghua.zheng@manchester.ac.uk

Abstract
Vehicular traffic is a major contributor to anthropogenic heat flux (AHF) in urban areas, amplifying urban heat island effects. However, few Earth system models explicitly represent traffic conditions and their associated heat emissions. This study introduces a new urban traffic module into the Community Earth System Model (CESM), enabling interactive simulation of traffic-related heat in urban areas. The module adopts a bottom-up approach to estimate traffic heat flux (Q_{traffic}) based on time-varying traffic volume and vehicle type distributions, while dynamically responding to meteorological conditions such as snow, rain, and low temperatures. Model validation was performed using observational data from two urban sites: Capitole of Toulouse, France (FR-Capitole), and Manchester, UK (UK-Manchester). At the FR-Capitole site, an annual mean Q_{traffic} of 22.23 W/m^2 in 2004 resulted in a simulated annual mean canopy air temperature increase of 0.4°C, improving the simulated turbulent heat flux compared to observations. At the UK-Manchester site, the simulation with a yearly mean Q_{traffic} of 16.27 W/m^2 showed a 0.25°C air temperature increase in 2022. These traffic-induced canopy warming also influenced the indoor environment, contributing to increased air conditioning use in summer and reduced building space heating demand in winter. This new functionality offers potential applications such as simulating traffic-induced AHF and its impacts on the climate system under future climate changes and transport transition scenarios.

Plain Language Summary

Urban traffic is a major source of anthropogenic heat, which can warm local thermal environments. However, most Earth system models (ESMs) do not include traffic-related anthropogenic heat in their simulations, so they fail to capture cities' real impact on the climate. In this study, we added a traffic module into the Community Earth System Model (CESM), an ESM that includes an urban climate model to explicitly represent and parameterize urban surface energy and water processes. The new module estimates traffic heat based on how traffic volumes and vehicle types change over time, allowing this heat to directly affect the urban climate modeling. We tested the model at two urban sites: the Capitole of Toulouse, France (FR-Capitole), and Manchester, UK (UK-Manchester), and compared the results with real-world data. The annual average traffic heat flux (Q_{traffic}) was 22.23 W/m^2 at FR-Capitole, leading to a 0.4°C increase in simulated air temperature in 2004. At UK-Manchester, incorporating a yearly mean Q_{traffic} of 16.27 W/m^2 raised the simulated air temperature by 0.25°C in 2022. Our results show that traffic-induced temperature changes varied across cities, and they should be considered in urban climate modeling.

1 Introduction

Anthropogenic heat flux (AHF) influences the Earth system through thermal circulation and the transboundary transport of air pollutants (Tao et al., 2021; M. Xie et al., 2016). Urban areas, the primary source of anthropogenic heat emissions, face growing risks from extreme heat and deteriorating air quality (Ryu & Min, 2024). AHF amplifies urban heat island (UHI) effect (Shahmohamadi et al., 2011), accelerates near-surface O_3 formation (M. Xie et al., 2016), and increases uncertainty in atmospheric stability (N. Zhang et al., 2010). Accurately modeling urban AHF is crucial for understanding and mitigating these impacts.

In urban areas, anthropogenic heat primarily originates from buildings, vehicular traffic, industry, and human metabolism, with the relative contributions varying across regions and time. For example, in Greater London, UK, from 2005 to 2008, buildings contributed 80% of total anthropogenic heat emissions, while traffic and human metabolism contributed 15% and 5%, respectively (Iamarino et al., 2012). Two Chinese cities, Chengdu and Chongqing, exhibited similar shares of anthropogenic heat emission in 2019, with traffic accounting for 26.9% and 28.5%, respectively (Ming et al., 2022). In Beijing, China, however, traffic contributed 30% of total emissions, representing the second-largest source after the building sector (45%), with industrial activities and human metabolism accounting for 20% and 5%, respectively (R. Sun et al., 2018). In São Paulo, Brazil, traffic's share was even higher, reaching 50% (Ferreira et al., 2011). In some urban areas, such as Toulouse, France (Pigeon et al., 2007), Daegu, South Korea (Kim et al., 2022), traffic has emerged as the dominant source of AHF and a major contributor to the UHI effect in summer. Although building space heating contributes significantly to AHF in winter, its influence diminishes in summer, when traffic becomes a relatively more dominant heat source. In addition, traffic increases road surface temperature. Chapman and Thornes (2005) reported a 1.5°C difference between inside and outside lanes of a busy UK motorway in winter.

At the global scale, AHF accounts for only about 1% of greenhouse gas forcing (Flanner, 2009). Because of its relatively small contribution, global climate models initially neglected it in global climate simulations (e.g., Hertwig et al., 2021). However, since the 1970s, numerical models have incorporated anthropogenic heat to assess its climatic effects (Block et al., 2004; Washington, 1972). Early global climate simulations prescribed AHF as a constant to assess atmospheric model sensitivities, neglecting its spatial heterogeneity and temporal variations (e.g., Block et al., 2004; McCarthy et al., 2010; Washington, 1972) (Figure 1). Flanner (2009) incorporated seasonal and diurnal cycles as weighting factors to refine the spatial and temporal variability of AHF, improving upon the annual mean constant approach. They demonstrated that incorporating AHF in the Community Atmosphere Model (CAM) coupled with a slab ocean model warmed the substantial atmosphere up to 0.9°C under an AHF of 0.19 W/m^2, advocating its integration into global climate models (GCMs). G. J. Zhang et al. (2013) and B. Chen et al. (2014) followed Sailor and Lu (2004)'s top-down approach and applied more realistic estimates of global anthropogenic heat based on present-day energy consumption and population. They focused on AHF-induced changes in atmospheric circulation in global simulations. Recognizing the seasonal dependence of building energy use and the daily and hourly variations in travel behavior, Sailor et al. (2015) applied detailed temporal profiles to scale heat emissions from buildings, traffic, and human metabolism.

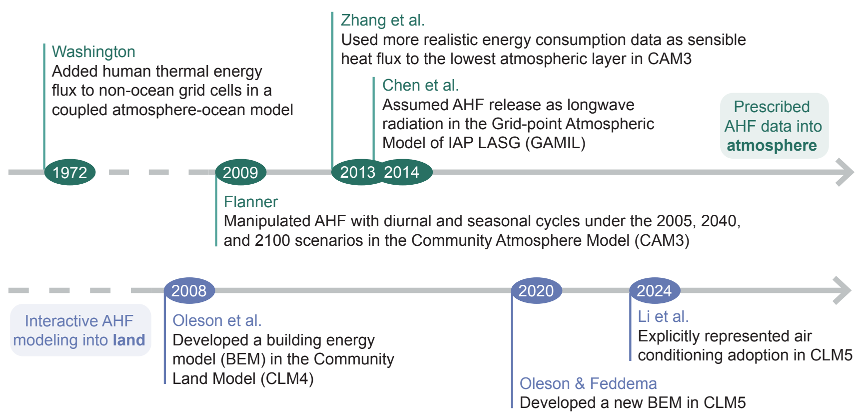

Figure 1. Timeline of incorporating anthropogenic heat in global climate simulation. Relevant references include: Washington (1972); Flanner (2009); G. J. Zhang et al. (2013); B. Chen et al. (2014); Oleson et al. (2008); Oleson and Feddema (2020); X. C. Li et al. (2024). The time axis is not regularly spaced.

Prescribing AHF entering the atmosphere does not directly influence the land surface, as it omits the connection to the land surface, nor does it differentiate between urban and non-urban areas. Moreover, transportation energy use may extend beyond urban vehicular traffic, potentially leading to a mismatch with the scope of urban traffic-related AHF. Over the past decades, the use of GCMs or Earth system models (ESMs) for large-scale urban climate studies has been increasing (e.g., Fischer et al., 2012; McCarthy et al., 2012; Y. Sun et al., 2024, 2025; Xia et al., 2025; Yu, Sun, et al., 2025; Yu, Zheng, et al., 2025; Zhao et al., 2021; Zheng et al., 2021). This advancement has motivated alternative approaches that explicitly represent anthropogenic heat release processes in urban areas within the land component of GCMs/ESMs. The Community Earth System Model (CESM) integrates a building energy model into its urban component, the Community Land Model-Urban (CLMU), to simulate building-related AHF (X. C. Li et al., 2024; Oleson et al., 2008; Oleson & Feddema, 2020). This is an online calculation of building space heating/cooling flux interactively based on indoor and outdoor temperature at each simulation time step (Bueno et al., 2012; F. Chen et al., 2011; Oleson et al., 2010). Here, "online" is defined as a process that is performed simultaneously within the main simulation, using the model's current state at each time step. However, considering only AHF from the building sector in CLMU may lead to an underestimation of its impact on urban climate and the broader climate system.

Due to the lack of real-time traffic input data and the limited representation and parameterization of urban surfaces at the global scale, vehicle-specific AHF has not yet been integrated within GCMs/ESMs. Instead, multiple regional simulations have incorporated traffic-related heat and assessed its thermal impacts. For example, Chow et al. (2014) highlighted the significance of vehicular traffic in modeling AHF and its contribution to the UHI effect using the Weather Research & Forecasting Model (WRF) with a multi-layer urban scheme, the Building Effect Parameterization (BEP), and the Building Energy Model (BEM), i.e., WRF-BEP/BEM. However, the performance of traffic heat modeling integration is not consistently better or pronounced (Ohashi et al., 2007; Juruš et al., 2016).

After reviewing the literature on approaches to modeling urban traffic heat (see Appendix B1), we found that a bottom-up approach makes it practical to implement online urban traffic heat modeling within the GCM/ESM framework. This approach provides greater specificity of local traffic conditions compared to conventional inventory-based methods, while also simplifying simulations by accounting for spatial resolution, modeling complexity, and computational cost. In this study, we incorporate an online traffic heat flux module into CESM and highlight two key advancements of our new traffic heat model. First, it represents spatio-temporally varying traffic volumes and vehicle type fractions, making it suitable for long-term climate simulations under both historical and future scenarios. Second, it dynamically responds to varying weather conditions, such as cold spells, rainfall, and snowfall, to more realistically represent the interaction between meteorology and traffic in a climate model. Third, it incorporates multiple vehicle types, including conventional internal combustion engine vehicles (ICEVs), hybrid-electric vehicles (HEVs), and electric vehicles (EVs), allowing it to reflect the impacts of future transitions to cleaner energy sources. These features enhance the model's potential for supporting future global urban climate adaptation efforts using CESM under transport transitions associated with Shared Socio-economic Pathway-Representative Concentration Pathway (SSP-RCP) scenarios.

This paper is organized as follows: Section 2 describes the parameterization scheme, model validation method, and sensitivity analysis design. Section 3 shows simulation outputs in comparison with observations at two sites. Section 4 discusses future directions of promoting the traffic module's application for larger scales. Section 5 summarizes key findings of simulated traffic-induced thermal effects.

2 Method and Data

2.1 Modeling Urban Traffic Flux

2.1.1 Inserting Traffic Heat Flux into the Urban Surface Energy Balance

Community Land Model-Urban (CLMU) is a single-layer urban canopy model designed within the framework of Earth system modeling. It represents urban land-units as tall building district (TBD), high-density (HD), and medium-density (MD) urban areas, excluding low-density built-up areas (Figure C1(a)). Each class of urban land-unit consists of five surface types: roof, sunlit wall, shade wall, pervious floor, and impervious floor. Details on the CLMU are described in Oleson and Feddema (2020).

The scope of urban traffic-induced heat includes only vehicular traffic on streets and roads within cities, and excludes broader transport outside the urban domain. To balance computational demands, traffic-related fluxes are represented as a simplified field, Q_{traffic}, excluding explicit parameterization of detailed heat-generation processes such as tire friction, radiative heat, and exhaust heat from vehicles. Q_{traffic} is added to the surface energy balance as a distinct term (Equation 1):

$$\begin{aligned} R_n &= SW_{\text{down}} - SW_{\text{up}} + LW_{\text{down}} - LW_{\text{up}} \\ &= Q_{\text{h}} + Q_{\text{le}} + Q_{\text{g}} - Q_{\text{ac}} - Q_{\text{w}} - Q_{\text{v}} - Q_{\text{traffic}}, \end{aligned} \tag{1}$$

where R_{n} is net radiation on urban surfaces (W/m^2), calculated as the balance between upwelling and downward radiation fluxes. Specifically, SW_{up} and SW_{down} are upwelling and downward shortwave radiation fluxes. LW_{up} and LW_{down} are upwelling and downward longwave radiation fluxes. The net energy from R_{n} is then partitioned into ground heat flux and turbulent heat fluxes. Q_{h} is sensible heat flux. Q_{le} is latent heat flux. Q_{g} is heat flux into soil or snow. Q_{ac} is the air conditioning flux for space cooling in buildings. Q_{w} is sensible heat flux from building space heating or cooling sources of urban waste heat, and Q_{v} is ventilation heat flux.

Q_{traffic} is calculated online at every model time step rather than being directly prescribed as input. Compared with the prescribed Q_{traffic}, the online approach makes the underlying source terms and equations explicit. This enables two-way interactions between meteorology and traffic during climate modeling. However, online urban traffic heat modeling inevitably increases computational cost and constrains model complexity. We do not explicitly partition traffic-related heat into sensible heat and latent components in Equation 1 for two reasons. First, latent heat accounts for only a small fraction of total heat emissions. For ICEVs, reported values range from 6.6% (Teufel et al., 2021), 7.3% (Iamarino et al., 2012), 8% (Khalifa et al., 2018), to 10% (Afshari et al., 2018). For HEVs and EVs, the latent heat contribution is even smaller. Thus, we represent traffic heat as a single term, Q_{traffic}, for simplicity. Second, we treat Q_{traffic} in the same manner as building-related heat terms (i.e., Q_{ac}, Q_{w}), which are separately included in the surface energy balance equation for downstream energy partitioning into turbulent heat fluxes (i.e., Q_{h}, Q_{le}).

The model assumes the AHF coming into the climate system from building energy consumption and urban traffic as (Equation 2):

$$\text{AHF} = Q_{\text{traffic}} + (Q_{\text{heat}} + Q_{\text{w}}), \tag{2}$$

where Q_{heat} is building space heating flux transferred from the indoor to the street canyon. Q_{traffic} represents traffic-related AHF and the sum of Q_{heat} and Q_{w} represents building-related AHF.

2.1.2 Estimating Vehicular Traffic Heat Flux

The Q_{traffic} depends on multiple parameters with different units and dimensions. It is estimated based on a bottom-up approach (Smith et al., 2009) (Equation 3):

$$\begin{aligned} Q_{\text{traffic}}(g,l,t) &= \frac{E_{\text{total}}}{A_{\text{improad}}} \\ &= \frac{E_{\text{vehicle}}(g,t)\cdot N_{\text{lane}}(g,l)\cdot Flow_{\text{vehicle}}(g,l,t)}{Speed_{\text{vehicle}}(g,t)\cdot Width_{\text{improad}}(g,l)\cdot 3600}, \end{aligned} \tag{3}$$

where g indexes a grid cell containing urban fraction, l indexes urban land cover class (TBD, HD, MD), t indexes simulation time step, E_{total} is the total traffic heat release rate (unit: W) on the impact area of impervious road A_{improad} (unit: m^2). The term "impervious" is used because traffic-related heat is released over paved, non-vegetated floor surface. In this context, A_{improad} represents the effective road area receiving vehicular heat. This distinction is made to separate it from the pervious floor, which represents urban vegetation. E_{vehicle} is the heat release rate per vehicle (W), N_{lane} is the number of vehicle lanes, $Flow_{\text{vehicle}}$ is the number of vehicles per hour per lane (vehicles/hour-lane), $Speed_{\text{vehicle}}$ is the vehicle speed (m/s), and $Width_{\text{improad}}$ is the width of impervious road.

N_{lane} is calculated as (Equation 4):

$$N_{\text{lane}}(g,l) = \begin{cases} 0, & \frac{Width_{\text{improad}}(g,l)}{Width_{\text{lane}}} < 0.5 \\ 1, & 0.5 \le \frac{Width_{\text{improad}}(g,l)}{Width_{\text{lane}}} < 2 \\ \left\lfloor \frac{Width_{\text{improad}}(g,l)}{Width_{\text{lane}}} \right\rfloor, & \end{cases} \tag{4}$$

where $Width_{\text{lane}}$ is a constant of 3.5 m. The floor function $\lfloor\rfloor$ returns the greatest integer less than or equal to a given number. If the result is an odd number larger than 1, 1 is subtracted to ensure an even number of lanes. As a result, N_{lane} can take values of 0, 1, 2, 4, 6, or 8, with maximum values of 8, 6, and 4 for TBD, HD, and MD areas, respectively. The remaining width ($Width_{\text{improad}} - Width_{\text{lane}} \cdot N_{\text{lane}}$) is assumed to be allocated to non-carriageway impervious road surface allocated to pedestrian-related features, including plazas, parking lots, and walkways.

$Width_{\text{improad}}$ is calculated as (Equation 5):

$$Width_{\text{improad}}(g,l) = \frac{H_{\text{roof}}(g,l)}{HWR(g,l)} \cdot (1 - F_{\text{perroad}}(g,l)), \tag{5}$$

where H_{roof} is the roof height, HWR is the canyon height-to-width ratio, and F_{perroad} is the fraction of pervious road. H_{roof}, HWR, and F_{perroad} are morphological parameters in CLMU, with values taken from CESM land surface datasets (`https://svn-ccsm-inputdata.cgd.ucar.edu/trunk/inputdata/lnd/clm2/`, last access: 29 November 2025). Although N_{lane} and $Width_{\text{lane}}$ could, in principle, be derived from real-world road network datasets such as OpenStreetMap (Haklay & Weber, 2008), we choose to use the CLMU's inherent morphological parameters to obtain N_{lane}. This approach allows us to maintain consistency with the urban representation in the model, rather than relying on potentially inconsistent or regionally variable external datasets. The default parameter dataset is derived from Jackson et al. (2010), and represents spatial variations of H_{roof} and HWR across 33 global regions and 3 urban land cover classes. Accordingly, the calculated $Width_{\text{improad}}$ and N_{lane} also vary by location g and urban land cover class l (Figure B1(a)–(c)). In addition, explicit road geometry is not required because CLMU represents urban areas as an idealized street canyon.

Except for these two morphological parameters (i.e., N_{lane}, $Width_{\text{improad}}$), the rest of the parameters (i.e., E_{vehicle}, $Flow_{\text{vehicle}}$, $Speed_{\text{vehicle}}$) are time-varying. Specifically,

E_{vehicle} is determined by the mix of vehicle types, including ICEVs using gasoline, diesel, HEVs, and EVs. The proportion of each vehicle type is shaped by technological advancements and policy regulations, and varies widely by region over time. For example, gasoline vehicles dominate in the U.S., diesel vehicles have historically been more common in Europe, and new-energy cars are rapidly gaining popularity in China (International Energy Agency (IEA), 2024). Accordingly, grouping fuels into gasoline and diesel captures major global preferences, while accounting for HEVs and EVs reflects their growing market shares. These variations highlight the importance of not relying on a single vehicle type assumption in GCMs/ESMs, as doing so would overlook critical regional differences in energy use and emissions. Accordingly, E_{vehicle} is weighted by the vehicle type fractions (Equation 6):

$$E_{\text{vehicle}}(g,t) = \frac{\sum_{v=1}^{4} p_v(g,t) \cdot E_v \cdot R_v}{\sum_{v=1}^{4} p_v(g,t)}, \tag{6}$$

where $p_v(t)$ indicates the fraction of a certain vehicle type v in a certain time, E_v indexes the total energy generation rate of a certain vehicle type v, R_v is the energy waste ratio, and the summation is over v=1,. . . ,4 for four vehicle types. By definition, $\sum_{v=1}^{4} p_v(t) = 1$. These four vehicle types do not represent usage categories such as passenger cars, buses, or light/medium/heavy commercial vehicles; rather, this is a simplification based solely on power source.

Vehicle energy profiles vary by vehicle types (Table 1). For ICEVs, energy generation is calculated as the product of the heat of fuel combustion (λ_{fuel}) and the fuel mass rate (m_{fuel}) in the engine ($E_v = \lambda_{\text{fuel}} \cdot m_{\text{fuel}}$) (Prusa et al., 2002). We assumed E_v for gasoline and diesel vehicles as 45 mJ/kg · 0.6 g/s = 27 kW, and 42.5 mJ/kg · 0.7 g/s = 29.75 kW, respectively. The net heat of gasoline combustion of 45 mJ/kg is derived from Sailor and Lu (2004), slightly lower than Smith et al. (2009)'s assumption of 45.85 mJ/kg. The heat combustion of 42.5 mJ/kg for diesel is derived from Lee et al. (2017), also lower than Smith et al. (2009)'s assumption of 46 mJ/kg. The E_v of EV at a vehicle speed range from 20 to 40 km/h is assumed at 5.6 kW (Ivanchev et al., 2020). This value is close to Y. Xie et al. (2020)'s estimation of energy consumption of 14.53 kWh/100 km at 25°C. HEV is assumed to be 40% of gasoline and 60% of electricity, leading to the E_v of 14.16 kW. We set R_v for gasoline and diesel as 0.7 and 0.65, respectively, as direct thermal loss accounted for more than 0.77 in a driving scenario of urban light snow (Prusa et al., 2002). According to Ivanchev et al. (2020), EV is six times more efficient than ICEVs, we set R_v as 0.12 for EV, closer to Ayartürk et al. (2016)'s estimation of up to 0.15. Compared to conventional ICEVs, the energy consumption of EVs is temperature-dependent (Skuza & Jurecki, 2022). We applied a time-varying temperature scaler SFT(g,t) to adjust EV's heat release to the air (Donkers et al., 2020; Y. Xie et al., 2020) (Equation 7):

$$\text{SFT}(g,t) = \begin{cases} 1.0 + 0.0165 \cdot (20 - T(g,t)), & 0 < T(g,t) < 20 \\ 1.33, & -10 < T(g,t) \le 0 \\ 1.4, & -20 < T(g,t) \le -10 \\ 1.58, & T(g,t) \le -20 \end{cases} \tag{7}$$

where t index model time, $T(g,t)$ is the grid-level atmospheric temperature (°C) at certain time of t.

Table 1. Vehicle Energy Profiles.

Vehicle type	Energy generation rate (E_v, unit: kW)	Energy waste ratio (R_v, unitless)	Vehicle heat release ($E_v \cdot R_v$, unit: kW)
Gasoline	27	0.7	18.9
Diesel	29.75	0.65	19.34
Hybrid electric	14.16	0.37	5.24
Electric	5.6	0.12	$0.67 \cdot \mathrm{SFT}$

[1] Final electric vehicle heat release is weighted by the temperature scaler (SFT) (Equation 7).

[2] We acknowledge that the estimation of E_v is based on the fuel economy of an average fleet. Actual energy consumption varies by vehicle type, powertrain characteristics, and operational conditions such as speed. Similarly, R_v of ICEVs may be lower in the future due to the improvements in fuel economy, potentially narrowing the difference between ICEVs and EVs.

[3] Users may customize the values of $E_v \cdot R_v$ based on specific vehicle fleet compositions or future technology scenarios to better suit their applications.

$Speed_{\text{vehicle}}$ is influenced by secondary weather impacts such as precipitation and snow. Rain and snow reduce road friction, leading to lower speeds due to cautious driving (Billot et al., 2009; Jägerbrand & Sjöbergh, 2016; Padget et al., 2001). Rakha et al. (2012) found that rain precipitation of 3 mm/h (∼0.00083 mm/s) and 15 mm/h reduced light-duty vehicle speed by 5% and 8%, respectively. C. Liu et al. (2017) found the average vehicle speed reduction of 6% when rain intensity was over 6.35 mm/h. Accordingly, the $Speed_{\text{vehicle}}$ is calculated as (Equation 8):

$$Speed_{\text{vehicle}}(g,t) = Speed \cdot \mathrm{SFRain}(g,t) \cdot \mathrm{SFSnow}(g,t), \tag{8}$$

where $Speed$ is set as a constant of 11.1 m/s (∼40 km/h), following the safe urban speed recommended by the World Health Organization (2018) and Pigeon et al. (2008). Here, $Speed$ is simplified as a fixed value, without accounting for variability across road types, traffic congestion levels, or different urban areas. Since the CLMU represents an urban area as a canyon, it does not distinguish road types such as local streets and highways. Its only consideration is the determination of thermal properties, e.g., asphalt and concrete. We fix the $Speed$ to maintain a consistent level of simplification in the urban representation.

SFRain is the scale factor used to adjust the $Speed$ based on atmospheric rain, and SFSnow is the scale factor used to adjust the $Speed$ based on atmospheric snow. The SFRain from Rakha et al. (2012)'s empirical experiments is (Equation 9):

$$\mathrm{SFRain}(g,t) = \begin{cases} 1.0 - 60 \cdot Rain(g,t), & 0 < Rain(g,t) \leq 0.00083 \\ 1.0 - (90 \cdot Rain(g,t) + 0.0425), & Rain(g,t) > 0.00083 \\ 1.0, & Rain(g,t) = 0 \end{cases} \tag{9}$$

where $Rain(g,t)$ is the atmospheric rain (mm/s) at certain time of t within the grid cell g. Based on C. Liu et al. (2017), SFSnow(t) is (Equation 10):

$$\mathrm{SFSnow}(g,t) = \begin{cases} 0.96, & 0 < Snow(g,t) \leq 0.000353 \\ 0.92, & 0.000353 < Snow(g,t) \leq 0.000706 \\ 0.91, & 0.000706 < Snow(g,t) \leq 0.00353 \\ 0.87, & Snow(g,t) > 0.00353 \\ 1.0, & Snow(g,t) = 0 \end{cases} \tag{10}$$

where $Snow$(t) is the atmospheric snow (mm/s) at certain time of t within the grid cell g.

$Flow_{\text{vehicle}}$ represents vehicle flow as a parameter varying with model time t and urban land-unit l. We introduced a scale factor $\mathrm{SF}(h)$ to represent diurnal variations of traffic flow (Equation 11):

$$Flow_{\text{vehicle}}(l,t) = \mathrm{AADT}(l,t) \cdot \mathrm{SF}(h), \tag{11}$$

where $\mathrm{AADT}(l,t)$ (unit: vehicles/day-lane) denotes the annual average daily traffic volume per lane in a certain urban land-unit l. $\mathrm{SF}(h)$ is the scale factor at hour h of the day. We have not considered the snowfall impact on vehicle flow yet, given the complex urban operations such as snow removal (Tanimura et al., 2015).

2.2 Model Modification and Configuration

As both a standalone land surface model and the land component of CESM, the Community Terrestrial Systems Model (CTSM) can not only operate in a land-only configuration driven by the data atmosphere model (DATM), but also be coupled with active atmospheric models, including the Community Atmospheric Model (CAM) or Weather Research and Forecasting (WRF) (CTSM Development Team, 2024; Mužić et al., 2025). Consequently, CLMU has been applied for multi-scale urban climate simulations under different configurations, ranging from global scales (e.g., Y. Sun et al., 2024; K. Zhang et al., 2025), to regional scales (e.g., C. Li et al., 2023; Wang et al., 2025) and local scales (e.g. Y. Sun et al., 2025; Yu, Sun, et al., 2025). Therefore, the traffic module can support multi-scale simulations in combination with CLMU. At this stage, we have developed the code and validated the functionality through single-point (one-grid-cell) simulations, but we have not yet prepared ready-to-use historical urban traffic parameter datasets or scenario-based traffic projection datasets for full regional and global applications. Developing such datasets and conducting larger-scale simulations will constitute a major task for future work. To facilitate testing of the module, example data and job scripts are provided for users' reference (Y. Sun & Zheng, 2025).

Model modification involves three processes: set-up, initialization, and computation (Figure 2). The new `UrbanVehicleType` module performs two key functions: reading time-varying traffic inputs and calculating Q_{traffic}. The traffic module adopts the `urban_traffic` namelist item to configure CTSM (Oleson & Feddema, 2020). The `urban_traffic` was originally implemented to serve as a placeholder for future development of a traffic heat model. It has been set to `.false.` in all previous versions of CTSM, excluding traffic heat from calculating urban surface energy balance (CTSM Development Team, 2025). At the model set-up stage, to enable the traffic module, users need to set `urban_traffic` as `.true.` and prepare a NetCDF file containing three-dimensional traffic input data (time, latitude, and longitude). This separate input file includes seven parameters, where `flow_*` denotes daily vehicle flow for three urban land-units (i.e., TBD, HD, and MD) and `fraction_*` denotes p_v for four vehicle types (i.e., gasoline, diesel, hybrid electric, electric). In practice, there is no restriction on the spatio-temporal resolution of `flow_*` and `fraction_*`, as it depends on the simulation period (subseasonal, yearly, or decadal) and the targeted climate scales (local, city, regional, or global). The traffic input data are customizable in both time step and spatial resolution. Temporal resolutions range from daily to decadal, and spatial resolutions range from kilometers to coarser grid spacing (e.g., 1°–2°).

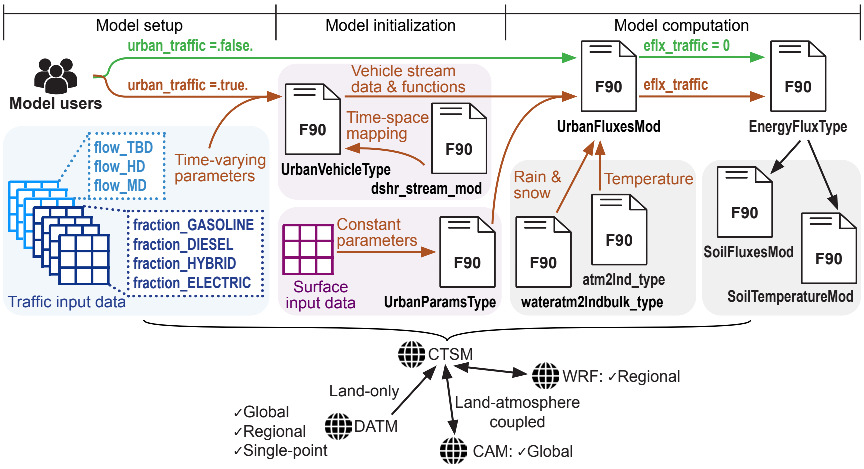

Figure 2. Workflow of incorporating urban traffic heat modeling in the Community Terrestrial Systems Model (CTSM). CTSM is the land component of the Community Earth System Model (CESM) and can be run in either land-only or coupled configurations. In land-only (offline) mode, CTSM is driven by atmospheric forcing data (DATM). In coupled (online) configurations, CTSM interacts directly with atmospheric models, including the Community Atmosphere Model (CAM) and the Weather Research and Forecasting (WRF) model. The required traffic input data consist of two types of parameters: the fractions of four vehicle types (`fraction_*`) and the daily traffic flows for three urban land cover classes (`flow_*`). These seven three-dimensional parameters, indexed by time, latitude, and longitude, are initialized and read as data streams, representing time-varying traffic conditions.

These traffic input parameters are not directly used in the computation; instead, they are first converted into data streams, a type of input that the model reads at runtime. The traffic module automatically maps them to the model time step via linear interpolation. Similarly, if the spatial domain of the traffic input data does not match that of the surface data, the module maps the values to the model grid by geographic location (latitude and longitude) using a nearest-neighbor approach. This spatio–temporal matching capability is implemented through the `dshr_stream_mod` module in the Community Data Models for Earth Prediction Systems (CDEPS) (`https://github.com/ESCOMP/CDEPS`, last access: 29 November 2025). The `dshr_stream_mod` module already supports several functionalities relying on data streams, such as the transient urban albedo representation (Y. Sun et al., 2024) and dynamic air conditioning adoption (X. C. Li et al., 2024). It provides flexibility for users to prepare traffic input.

At the model initialization stage, the `UrbanVehicleType` checks whether the traffic input files are valid. Meanwhile, the `UrbanParamsType` module initializes urban constant parameters from surface data. In the `UrbanParamsType` module, we incorporated new code to calculate N_{lane} and $Width_{\mathrm{improad}}$ based on Equation 4 and 5, respectively. At the model computation stage, the `UrbanFluxesMod` calculates the `eflx_traffic` (equivalent to Q_{traffic}) using the traffic data streams and supporting functions from `UrbanVehicleType`. The `eflx_traffic` is subsequently passed to `EnergyFluxType` for integration. It enters the canyon floor in `SoilFluxesMod`, thereby first influencing the ground (soil) temperature in `SoilTemperatureMod`. This approach differs from models where anthropogenic heat is directly added to the canyon air to affect air temperature directly, such as in the Common Land Model-Urban (CoLM-U) (`https://github.com/yuanhuas/CoLM-U/blob/master/main/UrbanFlux.F90`, last access: 29 November 2025) or added to the sensible heat flux, such as in WRF-SLUCM (`https://github.com/wrf-model/WRF/blob/master/phys/module_sf_urban.F`, last access: 29 November 2025).

2.3 Model Validation

We ran single-point simulations using CTSM (version tag `ctsm5.3.024`) for model validation at two sites, FR-Capitole (Section 2.3.1) and UK-Manchester (Section 2.3.2). Sites were selected based on the availability of both environmental measurements and traffic monitoring data (Table 2). Given that AHF cannot be measured directly, the simulated monthly mean AHFs at two sites were evaluated in comparison with a global monthly 1 km gridded anthropogenic heat dataset (AH4GUC) (Varquez et al., 2020). AH4GUC applies a top-down approach that scales energy consumption from regional or national totals to finer grid cells.

Table 2. Experiment Design.

Feature		Case study 1		Case study 2	
Site name		FR-Capitole (43.6035°N, 1.4454°E)		UK-Manchester (53.4827°N, 2.2336°W)	
City		Toulouse, France		Manchester, UK	
Köppen-Geiger climate zone (1991–2020) (Beck et al., 2023)		Cfa (Temperate, no dry season, hot summer)		Cfb (Temperate, no dry season, warm summer)	
Observation	Environmental measurement	Flux tower from the Urban-PLUMBER (Lipson et al., 2023)		HadUK-Grid 1 km observational dataset (Hollis et al., 2019; Met Office et al., 2025)	
	Environmental variables for model validation	Radiation and turbulent fluxes (i.e., SW_{up}, LW_{up}, Q_{h}, Q_{le}, Q_{tau})		Near-surface air temperature (T_{air}) and relative humidity (RH)	
	Traffic monitoring	A detector on the road from a global urban traffic flow dataset, UTD19 (Loder et al., 2019)		A VivaCity camera from Transport for Greater Manchester (TfGM)	
Simulation	Period for model spin-up	1 January 1994 to 20 February 2004		1 January 2012 to 31 December 2021	
	Period for data analysis	20 February 2004 to 28 February 2005		1 January 2022 to 31 December 2022	
	T_BUILDING_MIN	11.95°C		16.95°C	
	T_BUILDING_MAX	26.85°C		26.85°C	
	p_{ac}	0.047		0.018	
	Simulation name	CNTL	TRAF	CNTL	TRAF
	Traffic configuration	urban_traffic = .false.	urban_traffic = .true.	urban_traffic = .false.	urban_traffic = .true.

[1] T_BUILDING_MIN is the minimum interior building temperature, acting as a building space heating threshold to simulate Q_{heat}.
[2] T_BUILDING_MAX is the maximum interior building temperature, acting as a baseline threshold of air conditioning.
[3] p_{ac} is the air conditioning penetration rate. The simulated Q_{ac} is determined by both T_BUILDING_MAX and p_{ac} (X. C. Li et al., 2024).
[4] T_BUILDING_MIN, T_BUILDING_MAX and p_{ac} come from CTSM's default surface input data.
[5] CNTL refers to the control simulation using the default model source code. The TRAF simulation uses the same configuration as CNTL, except with the traffic heat module enabled.

2.3.1 Case Study 1: Capitole of Toulouse, France

The first site, FR-Capitole, is a flux tower site of Capitole, Toulouse, France (43.6035°N, 1.4454°E), with a 500 m observational footprint (Figure 3(a)). Its background climate is classified as temperate, with no dry seasons, and a hot summer (Beck et al., 2023). It is one of the 20 urban flux tower sites included in the Urban-PLUMBER model evaluation project (Lipson et al., 2023). The Urban-PLUMBER project provides local surface parameters for model configuration, along with radiative and turbulent flux observations for model evaluation.

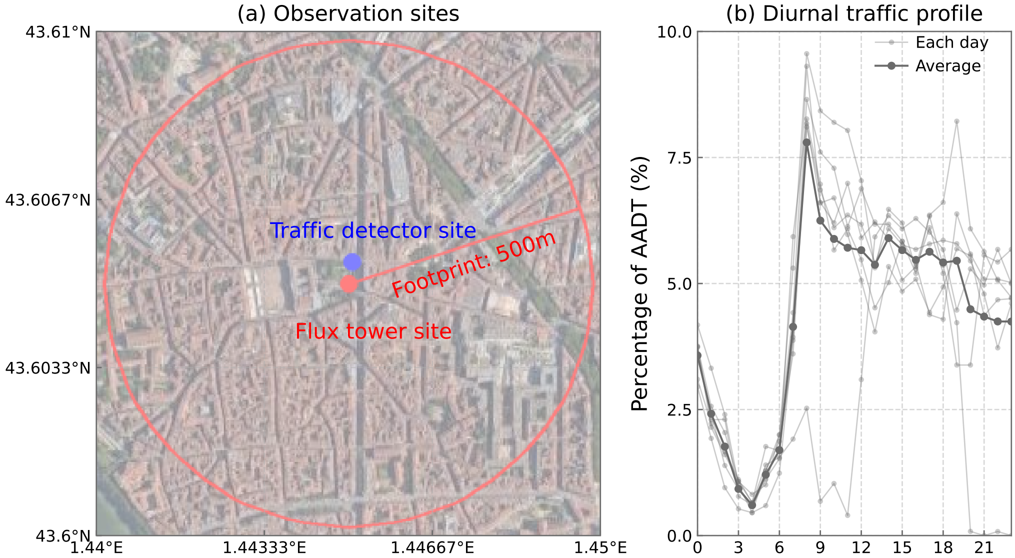

Figure 3. Case study of Capitole of Toulouse, France (FR-Capitole). (a) Observation site, with the background map imagery from © Google Maps satellite tiles. (b) Diurnal percentage of annual average daily traffic volume (AADT).

We matched this flux tower location with the nearest traffic detector (43.604907°N, 1.445499°E) from the UTD19 dataset (Loder et al., 2019). UTD19 measures hourly urban traffic in 40 global cities. The sensor detected traffic flow every Friday since 16 May 2008, for seven weeks at a 3-minute interval, providing vehicle volume per hour per lane. Daily traffic volume for these seven Fridays was 4939, 4475, 3853, 4405, 4664, 5059, and 3434 vehicles/day-lane, respectively. We calculated the AADT as 4404 vehicles/day-lane, and extracted the diurnal profile averaged from the UTD19 dataset, where the percentage of AADT peaked at 7.8% at 8:00 and dropped to the bottom at 0.6% at 4:00 (Figure 3(b)). This diurnal cycle was similar to Pigeon et al. (2007)'s, which ranged from a minimum of 0.4% at 03:00 to a maximum of 7.3% at 08:00 during weekdays based on 21 observation sites in Toulouse. We assumed the vehicle fleet composition in 2004 to consist of 40.6% gasoline, 59.4% diesel, 0% hybrid electric, and 0% electric vehicles. For comparison, the average passenger cars in use in France in 2019 were composed of 40.2% gasoline, 58.5% diesel, 0.7% hybrid electric, and 0.4% electric vehicles (European Automotive Manufacturers Association, 2021). $Width_{\mathrm{improad}}$ was 8.4 m and N_{lane} was 2.

Single-point simulations at the FR-Capitole site started from 1 January 1994 to 1 March 2005, where data for analysis began from 20 February 2004 (Goret et al., 2019; Masson et al., 2008). The model configuration and urban surface input in the CNTL simulation followed the established practices (Y. Sun et al., 2025). Specifically, the atmosphere data forced CTSM with a 30-minute interval. Urban morphological and albedo parameters were derived from the Urban-PLUMBER dataset, while the rest parameters were from CTSM5.3 default land surface input data (Table C1). As its local building height averaged around 15 m (Goret et al., 2019), we set the PCT_URBAN to 100% to represent a single medium-density urban land cover class. The building energy model within CLMU quantified Q_{ac} whenever indoor air temperature exceeds 26.85°C and Q_{heat}

whenever the indoor temperature drops below 11.95°C. The TRAF simulation differed from the CNTL simulation only by enabling the traffic module.

2.3.2 *Case Study 2: Manchester, UK*

We selected UK-Manchester as a second validation site, located at 53.4827°N, 2.2336°W, a commercial space closer to the Manchester city center (Figure 4(a)). The background climate is classified as temperate, with no dry season, and a warm summer (Beck et al., 2023). Traffic flow data came from a camera installed at 53.4802°N, 2.2323°W, supported by the Transport for Greater Manchester (TfGM) Vivacity platform. The AADT average based on hourly traffic volume in 2022 was 4697 vehicles/day-lane. As a commercial area, the diurnal cycle of the UK-Manchester site showed a peak hour at 17:00 (Figure 4(b)). $Width_{\mathrm{improad}}$ was 10.7 m and N_{lane} was 2. In 2022, the average car composition in the UK was 58.2% gasoline, 34.7% diesel, 4.9% hybrid electric, and 2.1% electric vehicles (European Automotive Manufacturers Association, 2024). However, the EVs share in Manchester remained at just 1% (Manchester City Council, 2022). Accordingly, we assumed the vehicle fleet to consist of 59.4% gasoline, 34.7% diesel, 4.9% hybrid electric, and 1.0% electric vehicles at the UK-Manchester site.

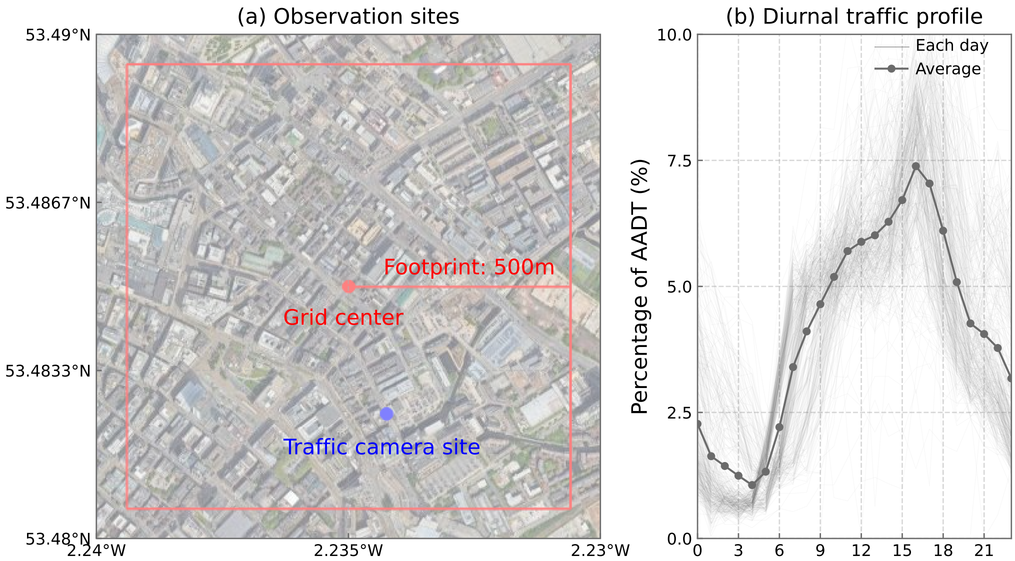

Figure 4. Case study of Dale Street, Manchester, UK (UK-Manchester). (a) A grid cell from the HadUK-Grid observational dataset, with the background map imagery from © Google Maps satellite tiles. (b) Diurnal percentage of annual average daily traffic volume (AADT).

In CNTL and TRAF simulations, the model spun up from 1 January 2012 to 31 December 2021, followed by one year for data analysis. Atmospheric forcings were derived from the ERA5-Land reanalysis data at an hourly interval, following the statistical bias-correction protocol described in L. Zhang et al. (2025). According to local climate zone classification, the site is classified as compact mid-rises, LCZ 2 (Demuzere et al., 2022). Thus, we set the PCT_URBAN as 100% for the medium-density class. The building height was 26 m, extracted from the Global Human Settlement Layer (GHSL) dataset (Pesaresi & Politis, 2023). Except for building height, the rest of the urban parameters came from the CTSM5.3 default surface input data (Table C1).

The model's performance was evaluated against the HadUK-Grid data from the nearest grid cell (Figure 4(a)). HadUK-Grid provides gridded climate observations for the UK, generated by interpolating in-situ measurements to a 1 km spatial resolution (Hollis et al., 2019; Met Office et al., 2025). We extracted the monthly mean near-surface air temperature (T_{air}) and vapor pressure, which was subsequently converted to relative humidity (RH) for model evaluation.

Given that the UK experienced record-breaking temperatures in the summer of 2022, we further examined how human heat stress was amplified by traffic-induced heat during urban heatwaves. A heatwave in Manchester is defined as at least three consecutive days with daily maximum temperatures exceeding 25°C (McCarthy et al., 2019). Two such heatwave events occurred at the UK-Manchester site, from 17 to 19 July and from 9 to 15 August 2022. Three human heat stress indicators were used to assess thermal comfort conditions, including the 2 m US National Weather Service Heat Index (NWS_HI), 2 m simplified Wet-Bulb Globe Temperature (sWBGT), and 2 m Discomfort Index (DI). NWS_HI is calculated as (Equation 12):

$$\begin{aligned}\mathrm{NWS\_HI} =& -42.379 + 2.04901523 \times T_{\mathrm{f}} + 10.14333127 \times \mathrm{RH} - 0.22475541 \times T_{\mathrm{f}} \times \mathrm{RH} \\ & - 6.83783 \times 10^{-3} \times T_{\mathrm{f}}^2 - 5.481717 \times 10^{-2} \times \mathrm{RH}^2 \\ & + 1.22874 \times 10^{-3} \times T_{\mathrm{f}}^2 \times \mathrm{RH} \\ & + 8.5282 \times 10^{-4} \times T_{\mathrm{f}} \times \mathrm{RH}^2 - 1.99 \times 10^{-6} \times T_{\mathrm{f}}^2 \times \mathrm{RH}^2,\end{aligned} \tag{12}$$

where T_{f} is the air temperature in Fahrenheit (°F), RH is the relative humidity (%). sWBGT is calculated as (Equation 13):

$$\mathrm{sWBGT} = 0.567 \times T_{\mathrm{c}} + 0.393 \times \frac{V_{\mathrm{p}}}{100} + 3.94, \tag{13}$$

where T_{c} is the air temperature (°C), V_{p} is the vapor pressure (Pa). DI is calculated as (Equation 14):

$$\mathrm{DI} = 0.5 \times T_{\mathrm{w}} + 0.5 \times T_{\mathrm{c}}, \tag{14}$$

where T_{w} is the 2 m wet-bulb temperature (°C). These indicators are computed by the `HumanIndexMod` in CTSM (Buzan et al., 2015).

2.4 Model Sensitivity Analysis

To evaluate the model's sensitivity to urban traffic heat, we conducted two idealized experiments that perturbed selected traffic parameters. One is to apply perturbation factors of ±10%, ±20%, ±40%, and ±80% to AADT. This sensitivity test did not consider roadway capacity constraints. It was not intended to represent realistic traffic flows, but rather to assess how the model responds to changes in traffic volumes. Another set of perturbations to p_v involved increasing the values for HEVs and EVs by 5%, 10%, 15%, 20%, 25%, and 30%, respectively, while reducing the corresponding values for gasoline and diesel vehicles. In other words, the corresponding reductions in ICEVs were 10%, 20%, 30%, 40%, 50%, and 60%. This experiment was intended to mimic scenarios of transport electrification (i.e., the shift from ICEVs to HEVs or EVs).

Simulations were performed for two representative weeks, one in summer and one in winter, at each study site. For the FR-Capitole site, simulations were carried out from 27 June to 4 July 2004 (summer) and from 2 January to 9 January 2005 (winter). For the UK-Manchester site, the simulation periods were from 16 July to 23 July 2022 (summer) and from 10 December to 17 December 2022 (winter). The results from the 8 AADT perturbations and 6 p_v perturbations, evaluated for the two periods at the FR-Capitole site, were compared against hourly observations and summarized using Taylor diagrams (Taylor, 2001). Taylor diagrams display the relationship between these datasets, illustrating the normalized standard deviation (σ), correlation coefficient (ρ), and centered root-mean square difference (E').

3 Result and Discussion

This section describes the results of model validation and sensitivity analysis. Section 3.1 and Section 3.2 show model validation results at FR-Capitole and UK-Manchester sites, respectively. Section 3.3 compares the different traffic-induced thermal impacts between the two sites. Section 3.4 summarizes variations of urban variables by perturbing traffic volumes and vehicle type fractions.

3.1 Traffic-Induced Thermal Effects at FR-Capitole

For simulations at the FR-Capitole site, the incorporation of urban traffic modeling showed great improvement of sensible heat flux (Q_{h}) (Figure 5(a), (b)). An annual mean traffic heat flux (Q_{traffic}) of 22.23 W/m^2 from February 2004 to February 2005 resulted in a 15.78 W/m^2 increase in simulated annual average Q_{h}. As Q_{h} in the CNTL simulation was generally underestimated, adding traffic heat narrowed the underestimation throughout the year and aligned well with the observed Q_{h}, particularly from May to October. This reduced the RMSE of the monthly mean Q_{h} from 29.6 W/m^2 in the CNTL simulation to 17.0 W/m^2 in the TRAF simulation, representing a 43% reduction in error. Latent heat flux (Q_{le}) also showed reduced RMSE, where Q_{le} in the TRAF simulation was higher than in the CNTL simulation by an annual average of 1 W/m^2 (Figure 5(c), (d)). In summer, Q_{le} in the TRAF simulation was lower than in the CNTL simulation, as indicated by negative ΔQ_{le} values. Q_{le} represented the energy used for water evaporation, which was primarily governed by moisture availability. Traffic-induced surface and near-surface warming increased ground (soil) temperature (T_{grd}) and near-surface air temperature (T_{air}), reducing relative humidity and surface moisture. This drier environment limited evaporation, thereby decreasing Q_{le}. In contrast, in cooler seasons when T_{grd} was more moderate, evaporation was less moisture-limited, allowing for an increase in Q_{le}, reflected in positive ΔQ_{le}. As the inclusion of traffic heat modeling increased the Q_{h}, the simulated Q_{tau} showed a slight rise (Figure 5(e), (f)). This impact on Q_{tau} remained minor, as Q_{tau} was primarily driven by surface roughness (Y. Sun et al., 2025). In addition, the upward solar radiation (SW_{up}) remained unaffected, as it is determined by the surface albedo (Figure 5(g), (h)).

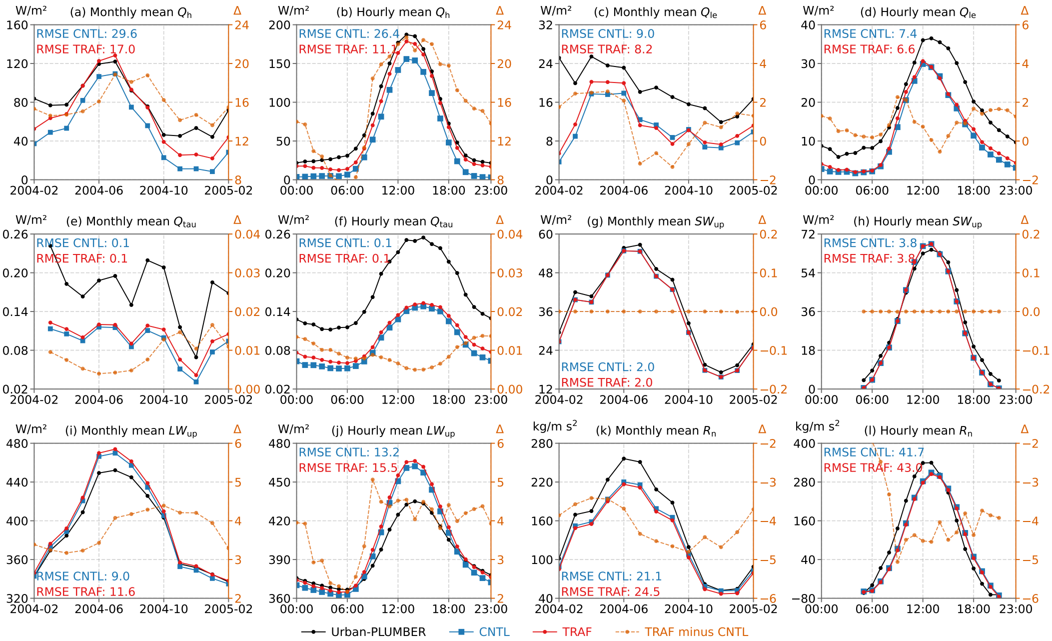

Figure 5. Monthly mean and hourly mean radiative, turbulent, and momentum fluxes in the CNTL and TRAF simulations at the FR-Capitole site, compared with observations from the Urban-PLUMBER project. (a)–(b) Sensible heat flux (Q_{h}). (c)–(d) Latent heat flux (Q_{le}). (e)–(f) Momentum flux (Q_{tau}). (g)–(h) Upward solar radiation (SW_{up}). (i)–(j) Upward longwave radiation (LW_{up}). (k)–(l) Net radiation on urban surfaces (R_{n}). Text on the top left is root-mean-square error (RMSE), measuring the average magnitude of the errors between modeled and observed values. RMSE closer to 0 is better. Some lines representing the CNTL and TRAF simulations overlap in the panels. The left y-axis shows the observed or modeled variables. The right y-axis shows the difference (Δ) between the TRAF and CNTL simulations.

Despite that adding traffic heat reduced the underestimation of Q_{h} and Q_{le}, the TRAF simulation showed higher longwave radiation flux (LW_{up}) (Figure 5(i), (j)) and lower net radiation flux (R_{n}) (Figure 5(k), (l)), particularly in summer, resulting higher RMSE compared to the CNTL simulation. Given that LW_{up} is determined by surface temperature, the overestimation of LW_{up} suggests that the surface is overheated. This is influenced by both model physics and parameters. Firstly, because the default emissivities assigned to impervious road and pervious road surfaces (0.97 and 0.99, respectively) are higher than the typical range of 0.9–0.95, LW_{up} was already overestimated in the CNTL simulation. With the added Q_{traffic}, the T_{grd} further increased, leading to higher LW_{up}. Using high-resolution urban parameters dataset such as U-Surf (Cheng et al., 2025) helps refine these estimates. Secondly, the underestimated Q_{le} was constrained by the simplified parameterization scheme for urban pervious surfaces, which omitted the transpiration effects of urban vegetation. Weak urban vegetation effect is likely to increase heat storage and warm the ground. This limitation has been acknowledged by previous studies (e.g. Y. Sun et al., 2025). Finally, Q_{traffic}, combined with building space heating flux (Q_{heat}), and waste heat flux (Q_{w}), was assumed to go into the urban canyon floor, warming the road surface before transferring the heat into the urban canopy air.

Adding Q_{traffic} showed notable increases in the simulated AHF, where the annual average AHF in the TRAF simulation was 27.91 W/m^2 and the maximum reached 85.53 W/m^2 on 28 January 2005 (Figure 6(a), (b)). Q_{traffic} of 22.23 W/m^2 contributed 80.2% of AHF (Figure 6(c), (d)). Comparatively, in the CNTL simulation, the annual average

AHF during 2004–2005 was 6.25 W/m^2, which only came from the building energy model. In the building sector, AHF mainly appeared in winter due to building space heating, where the daily mean building space heating flux (Q_{heat}) reached a maximum of 39.8 W/m^2 (Figure 6(g), (h)). Air conditioning heat flux was minimal and occurred primarily in the afternoon and at night, when the urban surface had absorbed heat during the day and indoor environments required cooling (Figure 6(f)). The traffic warming effect also influenced building energy consumption. In summer, more air conditioning and ventilation were required, where monthly mean Q_{ac} increased by up to 0.06 W/m^2 (Figure 6(e)) and Q_{v} by 0.15 W/m^2 (Figure 6(i)). In winter, less building space heating was required to maintain the indoor temperature above the model's critical threshold of indoor minimum temperature, where the monthly mean Q_{heat} was reduced by up to 2 W/m^2. The elevated canopy air temperature, combined with stable indoor temperature, narrowed the outdoor-indoor temperature gradient. This weakened the ventilation intensity, leading to a reduction in monthly mean Q_{v} by 0.3 W/m^2 in January 2005. Located in a temperate climate zone, FR-Capitole experienced a greater decrease in building space heating demand than an increase in air conditioning use in response to traffic-induced warming.

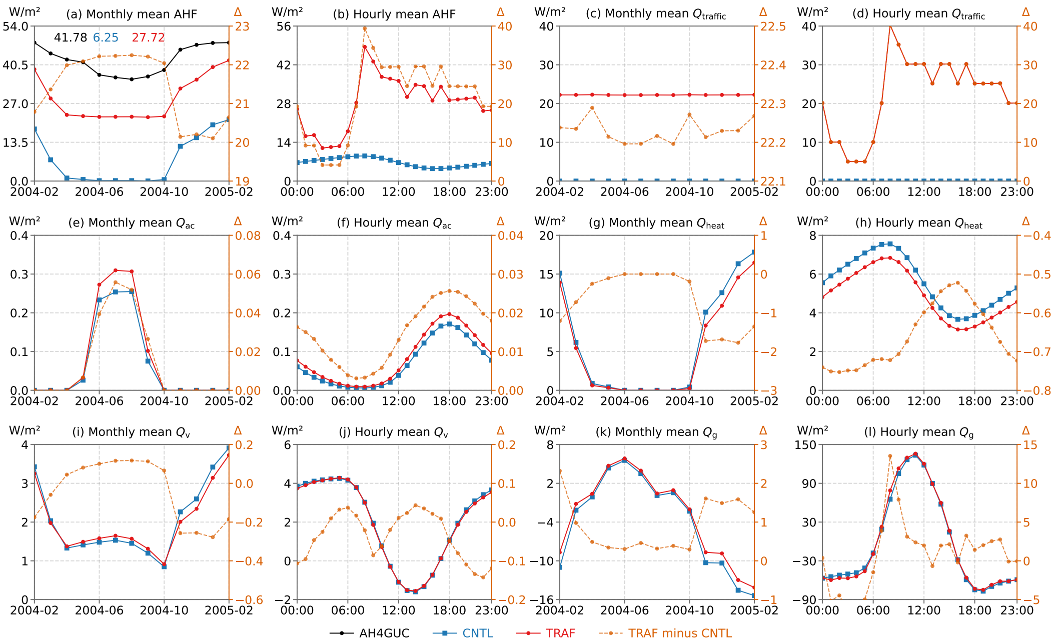

Figure 6. Monthly mean and hourly mean anthropogenic-related fluxes in the CNTL and TRAF simulations at the FR-Capitole site. (a)–(b) Anthropogenic heat flux (AHF). (c)–(d) Traffic heat flux (Q_{traffic}). (e)–(f) Air conditioning heat flux (Q_{ac}). (g)–(h) Building space heating flux (Q_{heat}). (i)–(j) Building ventilation flux (Q_{v}). (k)–(l) Heat flux entering the ground (Q_{g}). Some lines representing the CNTL and TRAF simulations overlap in the panels. The left y-axis shows the observed or modeled variables. The right y-axis shows the difference (Δ) between the TRAF and CNTL simulations. In panel (a), AH4GUC denotes values from the 1 km dataset for the 2010s (Varquez et al., 2021), and texts on the top left are the annual mean AHF from the AH4GUC product, CNTL simulation, and TRAF simulation, respectively.

The simulated AHF shows comparability with established datasets. For example, enabling traffic heat modeling computed a maximum monthly mean AHF of 41.23 W/m^2 in February of 2004–2005, closer to 48.22 W/m^2 from the AH4GUC for the 2010s (Figure 6(a)). Q_{traffic} contributed to 54.28% of AHF in February whereas more than 90% from April to October. However, Pigeon et al. (2007) found that AHF in the densest urban areas reached 100 W/m^2 in winter during 2004–2005. Such a high AHF has not been detected by the model at the FR-Capitole site yet. Given different approaches to estimate AHF, both simulations had lower monthly mean AHF than the AH4GUC dataset but were higher than Yang et al. (2017)'s 1 km AHF estimation of 0.1 W/m^2 based on nighttime light data in 2010.

Additionally, Q_{traffic} varied in response to weather conditions, enabling more accurate, event-driven AHF estimates. For instance, on 9 October 2004, heavy rainfall occurred at 17:00, with an intensity of 0.018 mm/s. According to Equation 8, this triggered the model to set the vehicle speed to zero. With no traffic activity, Q_{traffic} dropped to zero. Consequently, that day recorded the lowest daily mean Q_{traffic} value of 21.57 W/m^2. In contrast, the highest daily mean Q_{traffic} of 23.04 W/m^2 occurred on 25 October 2004, during which rainfall persisted from 10:30 into the night. Although vehicle speed was reduced under wet conditions, Q_{traffic} increased due to the continued traffic flow.

3.2 Traffic Impacts on Human Heat Stress during Heatwaves at UK-Manchester

The TRAF simulation demonstrates improved performance at the UK-Manchester site, as indicated by lower RMSEs of T_{air} and RH against observations compared to the CNTL simulation. Adding Q_{traffic} increased monthly mean T_{air} by 0.1–0.5°C (Figure 7(a)) and decreased RH by 1–3% (Figure 7(c)). Consequently, the TRAF simulation reproduced a warmer and drier urban environment. The difference in hourly mean T_{air} between the TRAF and CNTL simulation (ΔT_{air}) was higher at night than during the daytime (Figure 7(e)), suggesting peak traffic in the evening was likely to contribute to nocturnal warming. As a result, the RMSE of nighttime T_{air} between the HadUK-Grid and TRAF simulation was 0.46°C, which is lower than the corresponding value of 0.65°C in the CNTL simulation (Figure 7(d)). Magnitudes of monthly mean ΔT_{air} were larger in winter than in summer (Figure 7(a), (b), (d)), indicating a stronger seasonal sensitivity to traffic-induced warming under cooler background climate conditions.

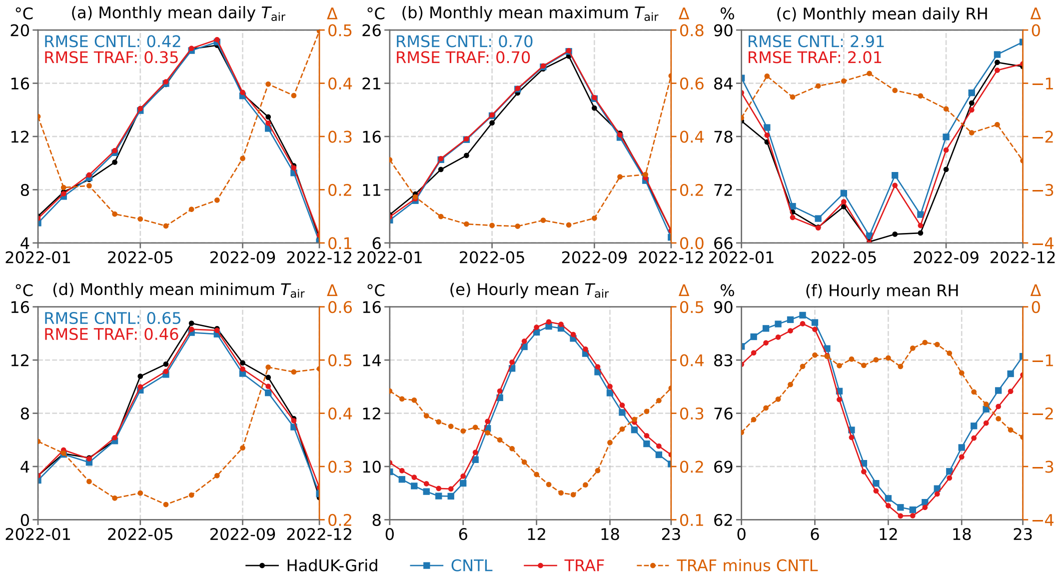

Figure 7. Monthly mean and hourly mean temperature and relative humidity in the CNTL and TRAF simulations at the UK-Manchester site, compared with observations from the HadUK-Grid dataset. (a) Monthly mean daily average 2 m air temperature (T_{air}). (b) Monthly mean daily maximum T_{air}. (c) Monthly mean daily relative humidity (RH). (d) Monthly mean daily minimum T_{air}. (e) Hourly mean T_{air}. (f) Hourly mean RH. HadUK-Grid provides monthly mean daily average, maximum, and minimum T_{air}, as well as daily average RH. The root-mean-square error (RMSE) measures the average magnitude of the errors between modeled and observed values. RMSE closer to 0 is better. The left y-axis shows the observed or modeled variables. The right y-axis shows the difference (Δ) between the TRAF and CNTL simulations.

Anthropogenic-related variables at the UK-Manchester site showed temporal variation patterns similar to those at FR-Capitole. TRAF simulations output an annual mean AHF to 25.86 W/m^2 (Figure 8(a), (b)), consisting of an annual mean Q_{traffic} of 16.27 W/m^2 (Figure 8(c), (d)). This was higher than the annual mean AHF from building energy consumption at 9.99 W/m^2 in 2022 in the CNTL simulation. For reference, Varquez et al. (2020) estimated an annual mean AHF of 21.4 W/m^2 for the 2010s and Jin et al. (2019) of 29.9 W/m^2 for 2015 (Table C2). However, both simulated AHFs were lower than Smith et al. (2009)'s estimation of 50–75 W/m^2 with an additional 8% from metabolism. Due to its colder background climate, the model simulated little air conditioning use in summer, even during the 16–19 July heatwave (Figure 8(e), (f)). In the model, the building space heating operated to maintain the indoor temperature above 16.95°C, which might be a relatively high threshold. Given the sparsely built-up area at the UK-Manchester site, the modeled indoor temperature might be lower due to greater heat loss, causing space heating to remain active longer than expected (Figure 8(g), (h)). As a result, uncertainties in modeling building space heating flux resulted in overestimated AHF in cold months. In December 2022, the monthly mean AHF was 41.1 W/m^2 in the TRAF simulation, higher than AH4GUC's monthly value of 22.6 W/m^2 in December (Figure 8(a)).

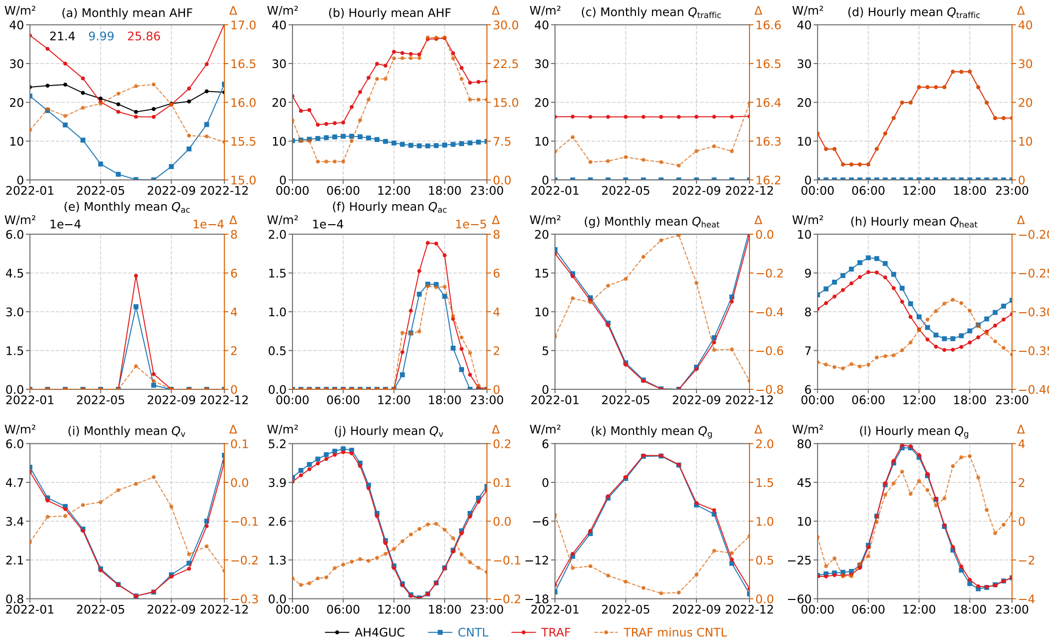

Figure 8. Monthly mean and hourly mean anthropogenic-related fluxes in the CNTL and TRAF simulations at the UK-Manchester site. (a)–(b) Anthropogenic heat flux (AHF). (c)–(d) Traffic heat flux (Q_{traffic}). (e)–(f) Air conditioning heat flux (Q_{ac}). (g)–(h) Building space heating flux (Q_{heat}). (i)–(j) Building ventilation flux (Q_{v}). (k)–(l) Ground flux (Q_{g}). Some lines representing the CNTL and TRAF simulations overlap in the panels. The left y-axis shows the observed or modeled variables. The right y-axis shows the difference (Δ) between the TRAF and CNTL simulations. In panel (a), AH4GUC denotes values from the 1 km dataset for the 2010s (Varquez et al., 2021), and texts on the top left are the annual mean AHF from the AH4GUC product, CNTL simulation, and TRAF simulation, respectively.

Traffic heat did not noticeably affect the heatwave duration, but it did intensify human heat stress during heatwave events. In the TRAF simulation, 2 m US National Weather Service Heat Index (NWS_HI) consistently exceeded that of the CNTL simulation, with ΔNWS_HI reaching a maximum of 4.9°C at 23:00 on 17 July (Figure 9(a)) and 5.3°C at 23:00 on 12 August 2022 (Figure 9(b)). This lag between the traffic peak and ΔNWS_HI peak stemmed from the natural properties of the urban surface, which absorbed heat during the day and released heat to the canopy air at night. Husni et al. (2022) also noted a temporal delay between traffic flow and its thermal impact on air temperature. Consequently, Q_{traffic} primarily added heat during the late afternoon, keeping canopy air warmer into the night. This reduced the day-night air temperature gradient, therefore elevating nighttime human heat stress during heatwaves. Comparisons between the TRAF and CNTL simulations showed that, during the July heatwave, the aggregated NWS_HI hours exceeding the critical “danger” threshold of 40°C increased by 1.9°C·hours. Interestingly, 2 m simplified Wet-Bulb Globe Temperature (sWBGT) and 2 m Discomfort Index (DI) in the TRAF simulation were occasionally lower than in CNTL during the late night and early morning (Figure 9(d), (f)). These reductions were likely due to decreased air moisture in the TRAF simulation, which had a stronger effect on these metrics than temperature during these times. Therefore, although traffic heat increased urban temperature, it did not always result in proportionally higher human heat stress, depending on the metric used and the timing of thermal effects.

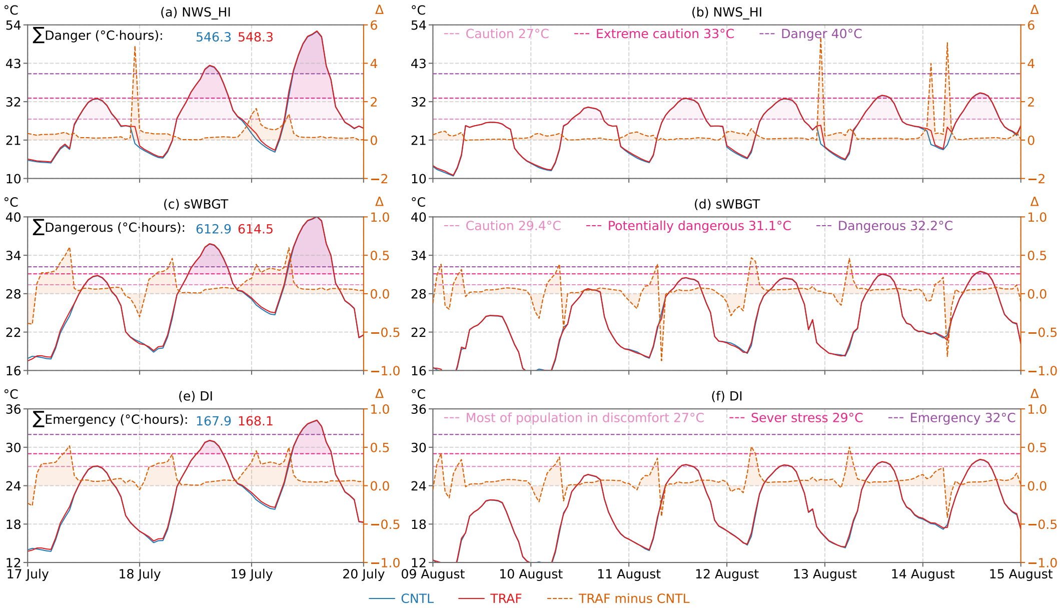

Figure 9. Heat stress variations during two heatwave periods in the CNTL and TRAF simulations at the UK-Manchester site. (a), (b) 2 m US National Weather Service Heat Index (NWS_HI). (c), (d) 2 m simplified Wet-Bulb Globe Temperature (sWBGT). (e), (f) 2 m Discomfort Index (DI). The left y-axis denotes the index values. The right y-axis denotes the differences between the TRAF and CNTL simulations. The text $\sum$ (unit: °C·hours) denotes the cumulative human heat stress burden, calculated as the product of each index and the number of hours exceeding its highest critical threshold.

3.3 Differences in Traffic Heat Impacts between FR-Capitole and UK-Manchester

Both FR-Capitole and UK-Manchester have similar annual average daily traffic volumes—4404 and 4697 vehicles/day-lanes. However, differences in vehicle type distributions lead to annual average Q_{traffic} values of 22.23 and 16.27 W/m^2, respectively. They showed traffic-induced urban warming with similar mechanisms but different temporal variations and magnitudes. Q_{traffic} added to the canyon floor first increases T_{grd} of impervious road and pervious road. This rise in T_{grd} enhances LW_{up} and reduces R_{n} under land-only mode (Figure 10). The elevated T_{grd} subsequently warms the canopy air. When the canopy air is warmer than the atmosphere, the increased T_{grd} enhances the temperature gradient between the canopy and the overlaying atmosphere, leading to an increase in Q_{h}. In contrast, during cold seasons in high-latitude regions, when the canopy air is colder than the atmosphere, Q_{h} becomes negative, and its absolute value decreases. Higher T_{air} also affects the indoor thermal environment by raising the T_{grd} of other surfaces (i.e., roof, sunlit wall, shade wall), and then T_{b}. In summer, the earlier exceedance of the indoor maximum temperature triggers the activation of Q_{ac} in the building energy model, increasing indoor cooling demands. In winter, the rise in T_{b} reduces the deviation from the setting of indoor minimum temperature, leading to lower space heating energy use. We acknowledge that this is an idealized scheme, unlike real-world conditions where traffic heat instantaneously influences road surface temperature through friction, radiation, and convection, and influences wall temperature through convection and radiation (Neog et al., 2021).

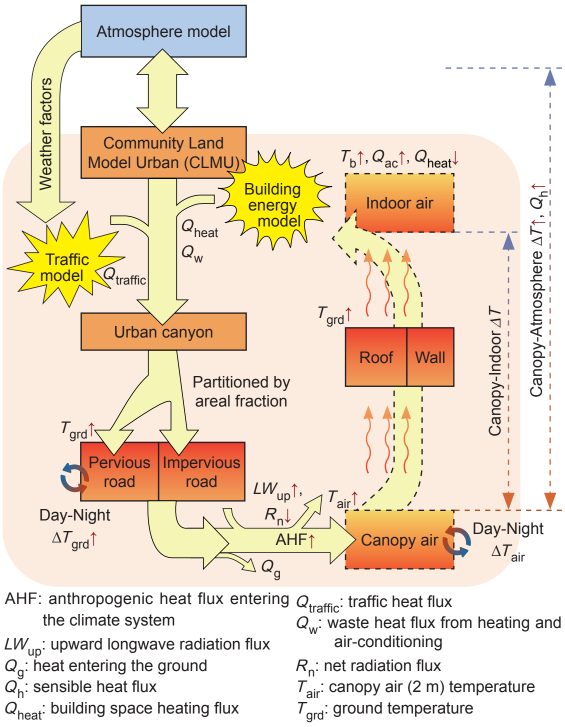

Figure 10. Biogeophysical mechanism of traffic-induced thermal effects based on model assumptions.

First, densely built-up areas were more likely to experience greater traffic-induced temperature increases compared to sparsely built-up areas under similar traffic volumes. During summer, FR-Capitole experienced a mean increase in ΔT_{air} of 0.3°C and an increase in indoor air temperature (ΔT_{b}) of 0.42°C when comparing the TRAF to CNTL simulations. The UK-Manchester site saw fewer ΔT_{air} of 0.16°C and ΔT_{b} of 0.14°C due to traffic heat, respectively (Table 3). From an urban morphological perspective, FR-Capitole is a densely built-up area, characterized by a canyon height-to-width ratio of 1.32, a high roof fraction of 0.62, and a small pervious road fraction of 0.26 (Table C1). These morphological parameters depicted a narrow canyon, dense buildings, and limited pervious roads, promoting greater heat retention within both the canyon and indoor spaces. In contrast, at UK-Manchester, the canyon height-to-width ratio is 0.75, the roof fraction is 0.35, and the pervious road fraction is 0.69 (Table C1). This combination of a wider canyon, lower building density, and higher pervious road fraction allows heat to dissipate more effectively. Consequently, the magnitude of temperature increases due to traffic at UK-Manchester was lower than at FR-Capitole. This morphological effect is also evidenced in Hong Kong, a typically highly dense urban area, where an average Q_{traffic} of 22.79 W/m^2 in January 2015 produced a ΔT_{air} of 0.35°C (X. Chen & Yang, 2022).

Table 3. Traffic-Induced Daily Mean Temperature Differences between the TRAF and CNTL Simulations.

Site name	FR-Capitole			UK-Manchester		
Year of simulation	2004			2022		
Traffic volume (unit: vehicles/day-lane)	4404			4697		
Metrics of simulation ouputs	ANN mean	JJA mean	DJF mean	ANN mean	JJA mean	DJF mean
Vehicle speed ($Speed_{\mathrm{vehicle}}$, unit: m/s)	11.08	11.09	11.08	11.06	11.08	11.03
Traffic heat flux (Q_{traffic}, unit: W/m^2)	22.23	22.2	22.24	16.27	16.24	16.33
Traffic-induced ground (soil) temperature increase (ΔT_{grd}, unit: °C)	0.64	0.58	0.69	0.38	0.29	0.46
Traffic-induced 2 m canopy air temperature increase (ΔT_{air}, unit: °C)	0.4	0.3	0.5	0.25	0.16	0.35
Traffic-induced indoor air temperature increase (ΔT_{b}, unit: °C)	0.27	0.42	0.0	0.05	0.14	0.0

[1] ANN, JJA, and DJF denotes annual, June-July-August, and December-January-February, respectively.

[2] Δ denotes the difference between the TRAF and CNTL simulations (TRAF – CNTL).

Second, increases in the traffic-induced ground temperature between TRAF and CNTL simulations (ΔT_{grd}) are directly influenced by traffic diurnal cycles (e.g., rush-hour peaks). ΔT_{air} exhibited a delayed response and was less strongly affected. ΔT_{b} exhibits smaller diurnal variations than both ΔT_{grd} and ΔT_{air}. During summer mornings at FR-Capitole, ΔT_{grd} and ΔT_{air} increased in parallel with the Q_{traffic} (Figure 11(a)). After the morning traffic peak subsided, ΔT_{air} declined moderately. At UK-Manchester, the evening traffic rush leads to nighttime warming, with ΔT_{air} peaking around 03:00 before decreasing as the accumulated heat is gradually released overnight (Figure 11(c)).

Third, seasonal climatic variations also influence the magnitude of traffic-induced temperature changes, reflecting differences in background meteorological conditions and building energy use. Given located in temperate climate zones, both sites displayed a bimodal pattern in wintertime ΔT_{grd} and ΔT_{air}, with peaks occurring around 10:00 and 23:00 (Figure 11(b), (d)). At UK-Manchester, diurnal mean ΔT_{air} reached 0.35°C in winter, twice the counterpart of 0.17°C in summer. Warmer air within the urban canyon contributed to reduced snow depth on urban surfaces, potentially affecting the timing and intensity of urban road de-icing operations. ΔT_{b} was close to 0°C at both sites, as the building energy model activated urban space heating to maintain T_{b} above the minimum threshold. The diurnal variation patterns of ΔT_{b} may differ in urban areas within tropical climates, where air conditioning is more dominant in regulating indoor temperature.

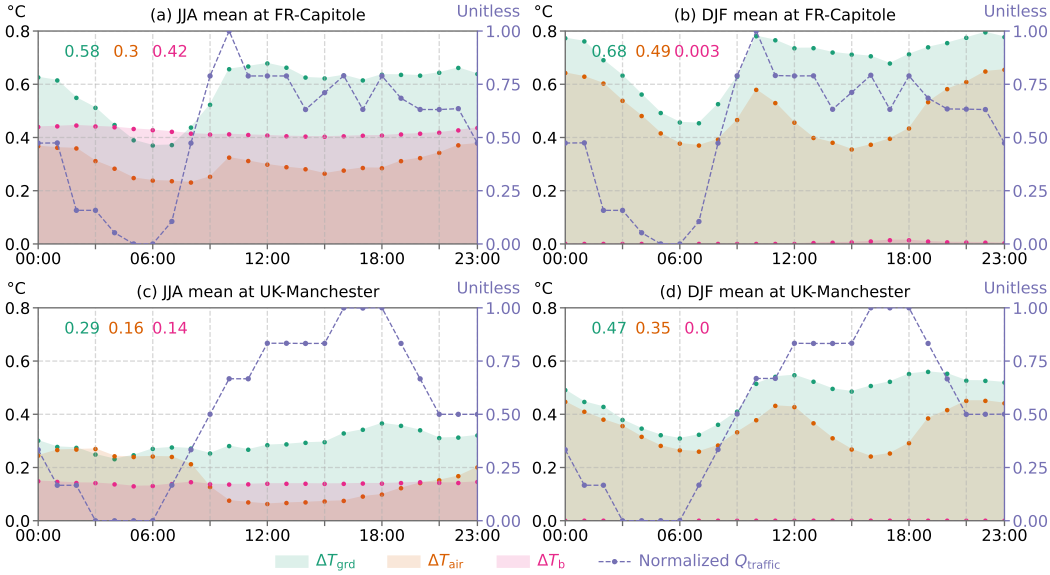

Figure 11. Diurnal variations (local time) of the differences in the ground (soil) temperature (ΔT_{grd}), 2 m canopy air temperature (ΔT_{air}), and indoor air temperature (ΔT_b) between the TRAF and CNTL simulations. (a) June-July-August (JJA) mean at FR-Capitole. (b) December-January-February (DJF) mean at UK-Manchester. (c) and (b) JJA and DJF mean at UK-Manchester, respectively. The right y-axis indicates the normalized traffic heat flux, ranging from 0 to 1. Texts on the top are the daily mean ΔT_{grd}, ΔT_{air}, and ΔT_b, respectively. The right y-axis indicates the difference (Δ) between the TRAF and CNTL simulations.

Overall, urban surface properties, traffic diurnal cycle, and background climate collectively shape the distinct temperature responses of the urban ground, canopy air, and indoor air between the two cities (Figure 12, 13). These differences highlight implications for both traffic management and urban heat management. Traffic-induced warming is more pronounced and persistent in compact built-up areas than in sparsely built-up areas. At FR-Capitole, heat from the morning traffic rush accumulates throughout the day and persists into the night. The day-night difference in ΔT_{air} is small: summer daytime ΔT_{air} reaches 0.29°C at 15:00, while nighttime ΔT_{air} remains at 0.25°C at 03:00, a difference of only a 0.04°C (Figure 12(a), (b)). At UK-Manchester, the evening rush intensifies nighttime warming. In summer, ΔT_{air} is 0.27 at 03:00, resulting in a relatively larger contrast of 0.2°C compared with the ΔT_{air} value of 0.07 at 15:00 (Figure 13(a), (b)). For cities with cold winters, traffic heat can provide moderate benefits by reducing the demand for space heating. However, this effect is limited: Q_{heat} decreases by only 1.4W/m^2 during the winter daytime (Figure 12(c)) and 1.6W/m^2 at night at FR-Capitole (Figure 12(d)), representing only about 10–20% of the average Q_{heat} (Figure 6(g)). Such reductions in Q_{heat} are even smaller at UK-Manchester, where ΔQ_{heat} accounts for only 2%–4% of the total (Figure 13(c), (d)).

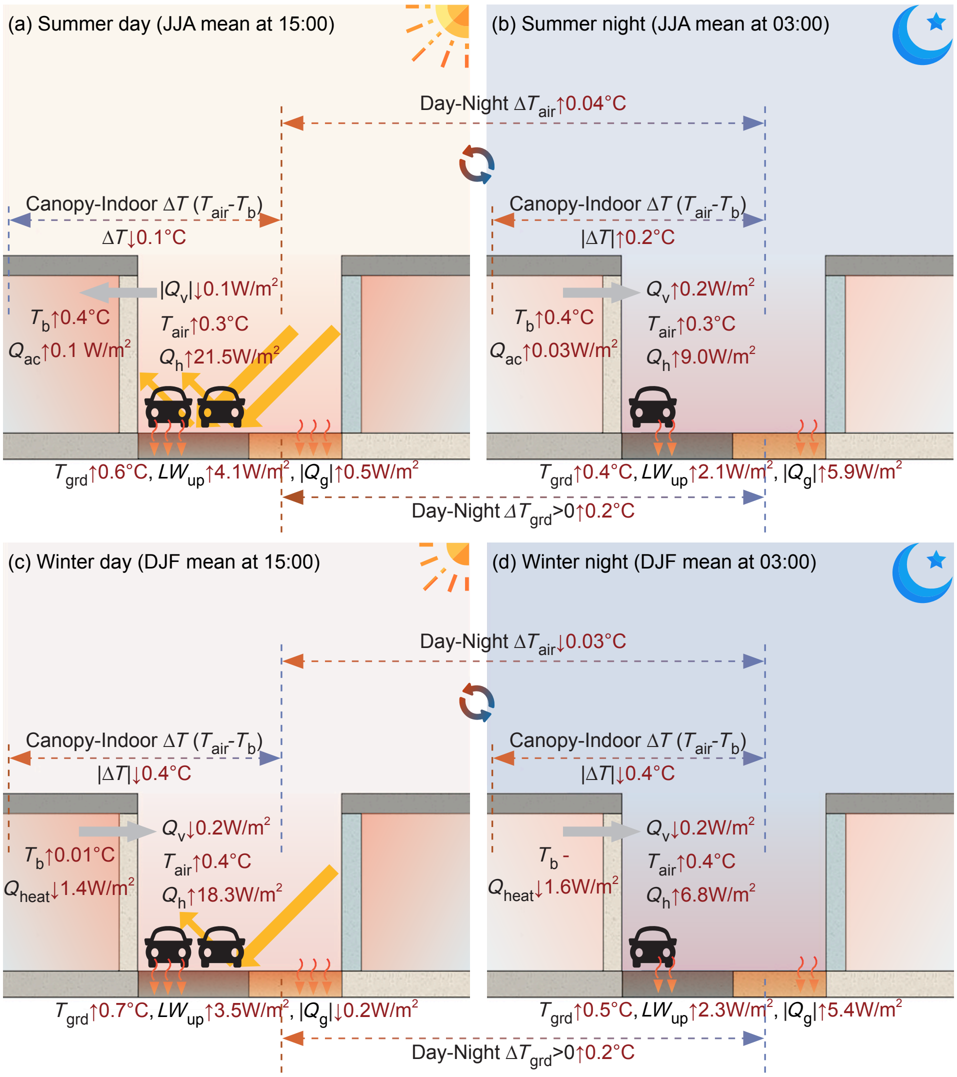

Figure 12. Traffic-induced changes in heat flux and temperatures at the FR-Capitole site in summer and winter, shown for 15:00 and 03:00 local time. The values represent differences between the TRAF and CNTL simulations. Red upward/downward arrows indicate increasing or decreasing trends, respectively. $LW_{\rm up}$ is upward longwave radiation. $Q_{\rm g}$ is the heat flux into the ground. $Q_{\rm heat}$ is the building space heating flux. $Q_{\rm ac}$ is air conditioning heat flux. $Q_{\rm v}$ is ventilation heat flux. $T_{\rm grd}$ is ground (soil) temperature. $T_{\rm air}$ is canopy air temperature. $T_{\rm b}$ is indoor temperature. | | denotes the absolute magnitude of negative values.

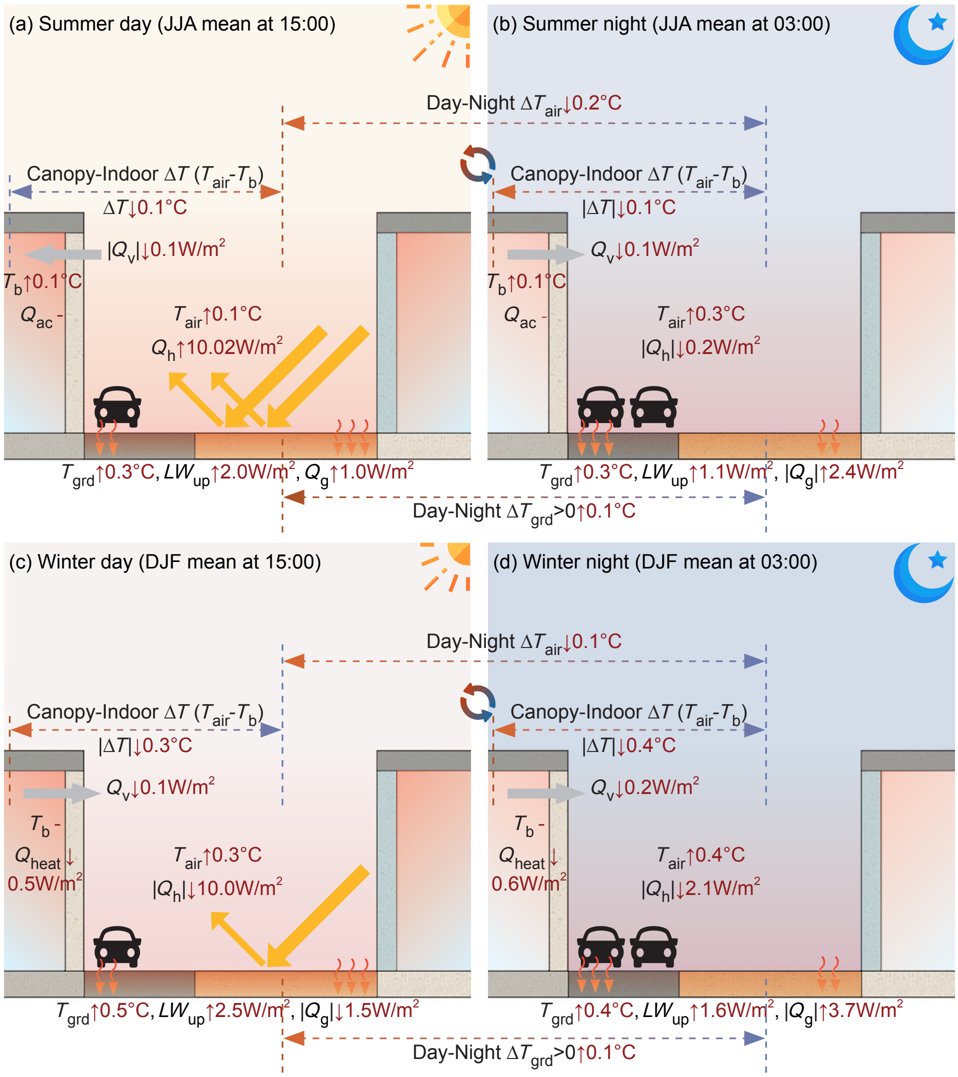

Figure 13. Traffic-induced changes in heat flux and temperatures at the UK-Manchester site in summer and winter, shown for 15:00 and 03:00 local time. The values represent differences between the TRAF and CNTL simulations. Red upward/downward arrows indicate increasing or decreasing trends, respectively. LW_{up} is upward longwave radiation. Q_{g} is the heat flux into the ground. Q_{heat} is the building space heating flux. Q_{ac} is air conditioning heat flux. Q_{v} is ventilation heat flux. T_{grd} is ground (soil) temperature. T_{air} is canopy air temperature. T_{b} is indoor temperature. | | denotes the absolute magnitude of negative values.

3.4 Seasonal Variations in Model Sensitivity to Traffic Heat Flux

At the FR-Capitole site, Q_{h} and Q_{le} were sensitive to AADT and p_v perturbations. In summer, normalized standard deviation (σ) of Q_{le} varied from 0.53 (−80% AADT) to 0.61 (+80% AADT) and σ of Q_{h} varied from 1.06 (−80% AADT) to 1.11 (+80% AADT) (Figure 14(a)). This suggested that increasing traffic volume provided more traffic-related AHF available to be partitioned into sensible and latent heat flux. σ of Q_{le} lower than 1 indicates that despite increasing AADT by 80%, the simulated Q_{le} variation was still lower than observations. Comparatively, LW_{up} and Q_{tau} showed limited sensitivity to changes in Q_{traffic}, with σ of 1.49 ± 0.006 and 0.53 ± 0.003, respectively. In winter, traffic heat became a negligible source of wintertime Q_h, with its σ ranging from 0.49 (−80% AADT) to 0.62 (+80% AADT) (Figure 14(a)), and from 0.51 (−60% ICEVs) to 0.55 (−10% ICEVs) (Figure 14(b)).

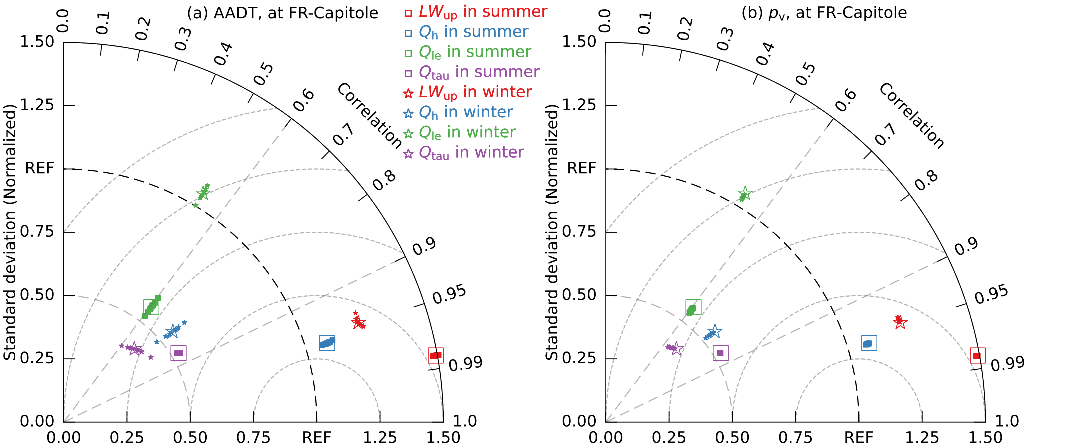

Figure 14. Taylor diagrams summarizing model sensitivity to traffic heat through parameter perturbations at FR-Capitole site. Panel (a) results from TRAF simulations in which perturbation factors of ±10%, ±20%, ±40%, and ±80% were applied to the annual average daily traffic volume (AADT). Panel (b) results from perturbations in vehicle type fraction (p_v), in which the fractions of gasoline and diesel vehicles decreased by 5%, 10%, 15%, 20%, 25%, and 30%, respectively, with corresponding increases applied to hybrid and electric vehicles. Variables include Upward longwave radiation (LW_up), sensible heat flux (Q_h), latent heat flux (Q_le), and momentum flux (Q_tau). Large symbols denote the results from the baseline TRAF simulation. "REF" denotes the reference dataset from observation. The radial distance between the origin and the symbols represents the normalized standard deviation (σ). σ close to 1 is better. The azimuthal position indicates the correlation between modeled data and observed data, with the correlation coefficient (ρ) denoted by the intersection between the radial line and the circle axis. ρ close to 1 is better. The contours centered on "REF" on the horizontal axis represent the normalized centered root-mean square difference (E'). E' close to 0 is better.

Given that traffic heat emission is also influenced by vehicle types, increasing HEVs and EVs portions show similar results from reducing traffic volume. At the UK-Manchester site, increasing the fractions of hybrid (+5%) and electric (+5%) vehicles (a total increase of 10%) results in a reduction of the daily average Q_traffic by 1.5 W/m^2 in winter, closer to the counterpart of 1.7 W/m^2 in the case of decreasing AADT by 10% (Figure 15(a)). Similarly, increasing the total fractions of HEVs and EVs by 60% reduces T_air from −0.17°C to −0.27°C, a decrease of 0.1°C in winter. For comparison, reductions of 0.08°C and 0.16°C were observed when AADT decreased by 40% and 80%, respectively.

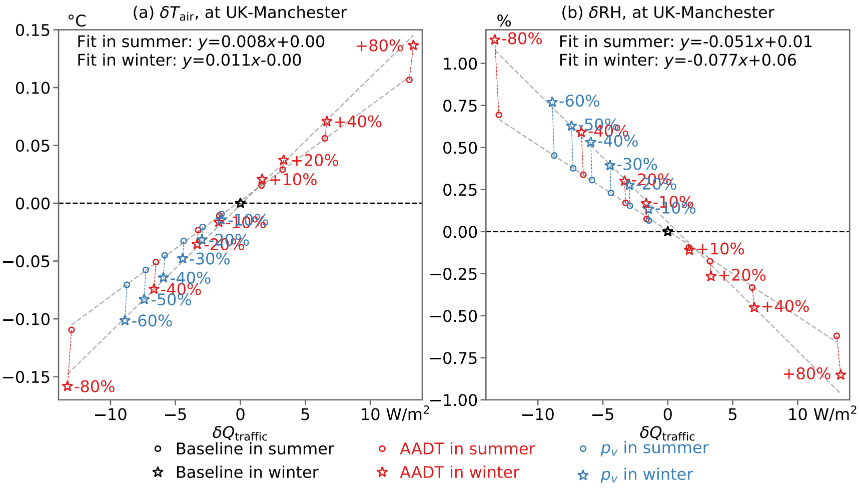

Figure 15. Correlation between changes in the simulated daily average traffic heat flux ($\delta Q_{\text{traffic}}$) and associated variations in (a) 2 m air temperature (δT_{air}) and (b) 2 m relative humidity (δRH). The annual average daily traffic volume (AADT) changed by ±10%, ±20%, ±40%, and ±80%. The fractions (p_v) of gasoline and diesel vehicles decreased by 5%, 10%, 15%, 20%, 25%, and 30%, respectively, corresponding to total internal combustion engine vehicles (ICEVs) decreases of 10%, 20%, 30%, 40%, 50%, 60%. The reductions are offset by increases in hybrid and electric vehicles. Gray dashed lines denote the linear regression fit.

Perturbations in AADT and p_v showed statistically near-linear relationship between changes in Q_{traffic} ($\delta Q_{\text{traffic}}$) and variations in T_{air} (δT_{air}) (Figure 15(a)), as well as between $\delta Q_{\text{traffic}}$ and variations in RH (δRH) (Figure 15(b)). According to Equation 3, Q_{traffic} depends linearly on both E_{vehicle} and the $Flow_{\text{vehicle}}$ in the numerator. This means proportional changes in either term lead to proportional $\delta Q_{\text{traffic}}$. By contrast, $Speed_{\text{vehicle}}$ and $Width_{\text{improad}}$ appear in the denominator; changes in these quantities can produce disproportionately large $\delta Q_{\text{traffic}}$, compared with equivalent relative changes in the numerator. For example, if the *speed* is reduced by 50% (from ∼40 km/h to ∼20 km/h) to mimic traffic congestion or adverse weather conditions while ideally maintaining the same vehicle energy consumption and traffic volume, then Q_{traffic} would approximately double. This is equivalent to the effect of doubling the AADT, leading to an increase in δT_{air} of around 0.15°C at the UK-Manchester site. Such speed-driven traffic warming is more pronounced and has been observed in Chicago, USA, where a 10 mph (∼16 km/h) reduction in bus speeds was associated with an increase of 0.36°C in surface UHI intensity (Lee & Berkelhammer, 2025).

4 Implications for Future Work

Single-point simulations at two European cities are designed for model validation; however, they do not yet fully demonstrate the new module's applicability at the regional and global scales. To move forward, future work involves both understanding model physics and enhancing data development. First, model validation should be conducted across additional sites representing diverse traffic conditions, background climate, and urban surface characteristics. For example, sensitivity experiments indicate that FR-Capitole and UK-Manchester sites are more sensitive to perturbations in AADT (annual average daily traffic volume) and p_{v} (the fraction of a certain vehicle type) during winter than in summer, as both are located in temperate climate zones. The seasonal variability in the traffic-induced thermal impact may not generalize to other urban areas in tropical or sub-tropical climates. X. Chen and Yang (2022) showed that simulated δT_{air} in Hong Kong, located in a sub-tropical and monsoon climate zone, was 0.35°C in January and 0.32°C in July 2015. The small winter-summer difference of 0.03°C indicates minimal seasonal variability, in contrast to the 0.2°C difference between the DJF mean and JJA mean ΔT_{air} observed at the FR-Capitole and UK-Manchester sites (Table 3). Further tests need to be conducted by employing multiple meteorological forcing ensembles to assess the model's climate sensitivity.

Second, to enable regional/global urban traffic heat modeling capability, it is essential to develop a dataset of AADT and p_v (Figure 16). A practical approach is to integrate established datasets from multiple sources, including large-scale open-access traffic observations (e.g., Gou et al., 2025; B. Li et al., 2024; Loder et al., 2019; Xu et al., 2024; van Strien & Grêt-Regamey, 2024), live traffic map platforms (e.g., Pokorný, 2017), and vehicle population reports and studies (e.g., European Automotive Manufacturers Association, 2021; Yan et al., 2024). Consistent with the coarse spatial resolution of GCMs/ESMs (e.g., 1°, 2°), the proposed global traffic input data require only relatively low spatial resolution or spatial variability. For instance, it could represent regional variability following the approach used in CESM, where default urban parameters vary across 33 global regions (Jackson et al., 2010). This type of representation differs from the continuous variability across grid cells used in high-resolution regional simulations. Meanwhile, for long-term climate projections, the required temporal resolution is relatively coarse, typically using yearly or decadal averages. In addition, the morphological parameter, $Width_{\mathrm{improad}}$ (impervious road width) may also need refinement by using global high-resolution urban parameter datasets such as U-Surf (Cheng et al., 2025) (Figure B1(d)) and GloUCP (Liao et al., 2025).

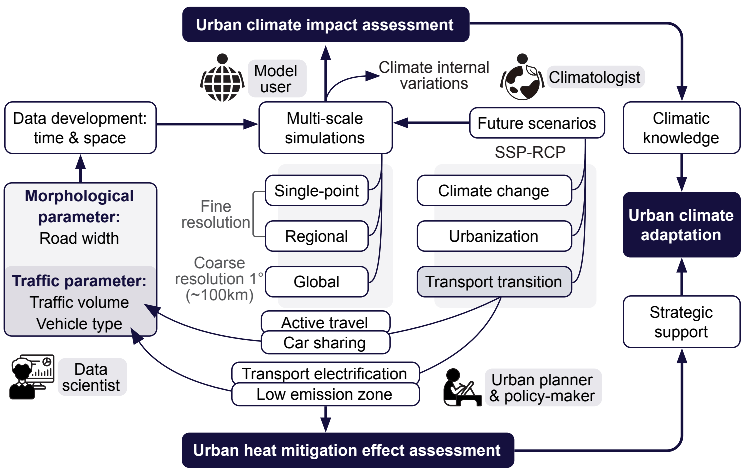

Figure 16. Illustration of future work on data development, and scenario-based urban climate projections using Community Earth System Model (CESM) with urban traffic heat modeling. Note that the spatial and temporal resolution of traffic parameters is scale-dependent: global simulations require relatively coarse resolutions (e.g., regional and annual variability), whereas single-point and regional simulations demand higher-resolution inputs (e.g., continuous spatial variability and monthly or daily traffic volumes).

Third, AHF derived from simulations using a bottom-up approach provides an alternative to existing AHF datasets obtained via top-down approaches. As the latter used to estimate monthly or yearly values (e.g., Dong et al., 2017; Jin et al., 2019; Varquez et al., 2021; Yang et al., 2017), the simulated AHF, along with the model time step, preserves realistic short-term variability, capturing diurnal and event-driven fluctuations. Such intercomparisons between simulated and inventory-based AHF estimation will help quantify uncertainties introduced by the building energy model and the newly implemented traffic module.

Lastly, the traffic module is intended to support future urban climate adaptation using Earth system modeling. CESM can currently represent both climate changes, defined by environmental variables such as radiative forcing and emissions, and urbanization, which reflect changes in urban land extent under different SSP-RCP scenarios (Gao & O'Neill, 2020; K. Zhang et al., 2025). The transport transitions for urban traffic are primarily related to SSPs, focusing on transport electrification policy and traffic demand management measures (e.g., car sharing, active travel) (Habib et al., 2020; Thomas, 2009; R. Zhang & Fujimori, 2020). Efforts are needed to project future AADT and p_v under different urban mobility and transport energy transitions associated with SSP-RCPs. For example, the on-road fleet scale under SSP2 (middle of the road) is larger than under SSP5 (fossil-fuel development) and SSP1 (green growth), reflecting disparities in demographic (population) and economic development (Shui et al., 2024). Meanwhile, SSP2, characterized by higher CO_2 emissions than SSP1 and SSP3 (regional rivalry), assumes the absence of EV policies and climate mitigation efforts (R. Zhang & Fujimori, 2020). In contrast, SSP1 is projected to have a high share of EVs up to 75% (Righi et al., 2023). Coupling climate and transport projections would further enable the assessment of heat mitigation strategies associated with the urban transport sector, such as the implementation of low emission zones in urban planning (Holman et al., 2015) and promoting active travel through walking and cycling. Ultimately, the blueprint aims to engage a broader community, including urban planners and policy-makers, in addition to the natural science and modeling community.

5 Conclusion

This study introduces a traffic module into the Community Earth System Model (CESM) for modeling traffic heat flux in urban areas. In the context of the urban surface energy balance, a variable representing traffic heat flux (Q_{traffic}) is added at the canyon floor, where the energy is subsequently redistributed, first warming the ground, then the canopy air, and finally the indoor air. The module was validated by conducting control (CNTL) and traffic (TRAF) simulations at the Capitole of Toulouse, France (FR-Capitole), and Manchester, UK (UK-Manchester) sites with measured data.

At the FR-Capitole site, incorporating an annual mean Q_{traffic} of 22.23 W/m^2 in 2004 increased the simulated annual averages of sensible heat flux (Q_{h}) by 15.78 W/m^2. RMSE of monthly mean Q_{h} between the TRAF simulation and observation was reduced to 17.0 W/m^2, lower than RMSE in the CNTL simulation of 29.6 W/m^2. At the UK-Manchester site, an annual mean Q_{traffic} of 16.27 W/m^2 in 2022 also produced better air temperature (T_{air}) and relative humidity. It increased T_{air} by 0.16°C in summer, whereas by 0.35°C in winter. Traffic-induced warming influenced not only temperature but also moisture, contributing to variations in human heat stress metrics. It increased the 2 m US National Weather Service Heat Index (NWS_HI), a temperature-driven metric, causing it to exceed the critical threshold of danger (40°C) by a cumulative 1.9°C·hours during the July 2022 heatwave at UK-Manchester. However, the 2 m Simplified Wet-Bulb Globe Temperature (sWBGT) and 2 m Discomfort Index (DI) occasionally decreased due to reduced humidity associated with traffic-induced drying.

Despite similar annual average daily traffic volume at FR-Capitole and UK-Manchester, the resulting thermal impacts varied. During summer, daytime T_{air} at 15:00 increased by 0.29°C at FR-Capitole, compared to only 0.07°C at UK-Manchester. This difference is attributed to denser building configurations, a narrower canyon, and less pervious road surfaces at FR-Capitole. Nighttime T_{air} at 03:00 increased by 0.25°C at FR-Capitole, comparable to the 0.27°C rise simulated at UK-Manchester. Due to a roof fraction and canyon height-to-width ratio at FR-Capitole nearly twice those of UK-Manchester, indoor temperature increases were more pronounced—0.42°C during summer nighttime at FR-Capitole versus 0.14°C at UK-Manchester. The lower building density at UK-Manchester facilitated greater heat dissipation, mitigating indoor warming. Overall, traffic-induced thermal effects are stronger in densely built environments where heat becomes trapped within the canyon and buildings. The diurnal traffic profile also plays a role, with higher evening traffic volumes likely contributing to prolonged nighttime warming, particularly during summer. Sensitivity analysis further showed that models were more sensitive to perturbations in traffic volumes and vehicle type fractions in winter than in summer. Given that both FR-Capitole and UK-Manchester were located in the template climate zone, the urban environment has limited downward energy in winter, where traffic sensible heat becomes a non-ignorable heat source.

This module was designed with careful consideration of multiple factors such as spatial resolution, model complexity, and computational cost, making trade-offs to balance model detail and computational efficiency within the Earth system modeling framework. Comparisons between the TRAF and CNTL simulations showed a moderate increase in runtime, observed in both the initialization process (Figure C2(a)) and the land model execution (Figure C2(b)). Controlling computational load comes at the expense of representational accuracy. The traffic module assumes fixed heat release rates across vehicle types, without accounting for their spatio-temporal variability. It operates under the assumption of a uniform vehicle speed, regardless of road types. It also simplifies vehicle classification into four categories based on power sources, without considering differences in vehicle usage patterns such as passenger cars, buses, and trucks. These simplifications of highly heterogeneous urban traffic are consistent with conventions in GCMs/ESMs, designed to reduce the difficulty of input data preparation and computational demand, thereby ensuring a more user-friendly implementation within Earth system modeling.

Appendix A Abbreviation and Acronyms

Table A1 lists the relevant variables used to describe the urban thermal environment, including fluxes, temperatures, and human heat stress indicators.

Table A1. Environmental Variable Definition.

Variable name	Long name	Unit	Source
AHF	Anthropogenic heat flux	W/m^2	Equation 2
Canopy-Indoor ΔT	Difference between T_{air} and T_{b}	°C	T_{air} minus T_{b}
Day-Night ΔT_{air}	Difference in T_{air} between day and night	°C	T_{air} at 15:00 minus T_{air} at 03:00
Day-Night ΔT_{grd}	Difference in T_{grd} between day and night	°C	T_{air} at 15:00 minus T_{air} at 03:00
DI	2 m discomfort index	°C	CTSM output
LW_{down}	Downward longwave radiation	W/m^2	CTSM output
LW_{up}	Upward longwave radiation	W/m^2	CTSM output
NWS_HI	2 m US National Weather Service Heat Index	°C	CTSM output
Q_{ac}	Air conditioning flux for building space cooling	W/m^2	CTSM output
Q_{g}	Heat flux into the ground	W/m^2	CTSM output
Q_{h}	Sensible heat flux	W/m^2	CTSM output
Q_{heat}	Building space heating flux	W/m^2	CTSM output
Q_{le}	Latent heat flux	W/m^2	CTSM output
Q_{tau}	Momentum flux	$kg/m\ s^2$	CTSM output
Q_{traffic}	Traffic heat flux	W/m^2	CTSM output
Q_{v}	Building ventilation flux	W/m^2	CTSM output
Q_{w}	Building waste heat flux	W/m^2	CTSM output
RH	2 m relative humidity	%	CTSM output
R_{n}	Net radiation flux	W/m^2	Equation 1
sWBGT	2 m simplified Wet-Bulb Globe Temperature	°C	CTSM output
SW_{down}	Downward solar radiation	W/m^2	CTSM output
SW_{up}	Upward solar radiation	W/m^2	CTSM output
T_{air}	2 m air temperature	°C	CTSM output
T_{b}	Building indoor temperature	°C	CTSM output
T_{grd}	Ground (soil) temperature	°C	CTSM output
ΔT_{air}	Difference in 2 m air temperature between the TRAF and CNTL simulations	°C	T_{air} from TRAF minus T_{air} from CNTL
ΔT_{b}	Difference in indoor air temperature between the TRAF and CNTL simulations	°C	T_{b} from TRAF minus T_{b} from CNTL
ΔT_{grd}	Difference in ground (soil) temperature between the TRAF and CNTL simulations	°C	T_{grd} from TRAF minus T_{grd} from CNTL

Appendix B Approaches to Modeling Urban Traffic Heat

B1 Literature Review

Urban climate models have incorporated traffic heat emission using three main approaches: top-down, bottom-up, and physical-process-based approaches. In a top-down approach, traffic heat is estimated from an energy-inventory perspective (e.g., Sailor & Lu, 2004), for example, (Equation B1):

$$Q_{\text{traffic}} = \text{pcDVD} \cdot \text{EneV} \cdot F \cdot pop, \tag{B1}$$

where pcDVD is per capita Daily Vehicle Distance (km/person day), F is hourly fractional traffic profile (%), pop is the hourly population density (person/km^2), and EneV is energy release per vehicle per meter (J/m). A bottom-up approach relies on local vehicle data such as traffic volume, vehicle types, and road types (e.g., Smith et al., 2009), for example,

$$Q_{\text{traffic}} = \frac{N_{v,r} \cdot \frac{L_r}{S_r} \cdot EF_{v,r} \cdot \lambda_v}{A}, \tag{B2}$$

where v indexes vehicle types, r indexes road, $N_{v,r}$ is the number of vehicles of type v on road r, L_r is the road length (m), S_r is the vehicle speed (m/s), $EF_{v,r}$ is the emission function per vehicle and road (g/km), λ_v is the net heat generated of fuel combustion (kJ/g) and A is the impact area (m^2). A physical-process-based approach is more complex, incorporating detailed parameterizations of vehicle-induced changes in radiation and wind, along with additional heat from tire friction to the road and exhaust emissions to the air (e.g., Xiao et al., 2018).

Integrating traffic heat into urban climate models varies in complexity (Table B1). For instance, the Town Energy Balance (TEB) model initially prescribed traffic-related AHF using a fixed annual average value of 8 W/m^2, scaled by a diurnal cycle, in a case study of Toulouse, France (Pigeon et al., 2008). This estimate was derived from surface energy balance measurements (Pigeon et al., 2007). Later, Khalifa et al. (2016) refined traffic heat estimation in TEB using two approaches. One was explicit urban traffic representation, incorporating real-time urban traffic characteristics such as traffic volume, vehicle speed, and subsequent energy consumption to estimate sensible and latent heat fluxes. The other was process-based parameterization, accounting for not only turbulent heat fluxes but also radiation and momentum fluxes. It incorporated detailed biogeophysical interactions with ambient conditions (e.g., radiation, temperature, wind). Such a process-based approach involves complex parameterization and computational demands and has typically been applied at the microscale, relying on empirical studies (Fujimoto et al., 2012). In addition, Bohnenstengel et al. (2014) incorporated transport-movement profiles into the Met Office–Reading Urban Surface Exchange Scheme (MORUSES) to convert daily energy demand into vehicle-related AHF.

Table B1. Estimating Traffic Heat Flux in Urban Climate Modeling.

Reference	Urban climate model	Urban climate scale	Method of traffic-related AHF	Traffic heat	Traffic-induced thermal effects	Follow-up studies (e.g.)
Ohashi et al. (2007)	CM-BEM	Local	Bottom-up estimation	Up to 100 W/m^2 (weekday) and 40 W/m^2 (holiday) in the evening hours of Kanda area, Tokyo, Japan	Overestimated near-surface air temperature by using the maximum traffic volume	Kikegawa et al. (2014); Takane et al. (2022)
Pigeon et al. (2008)	TEB	Local	Surface energy balance measurements	Annual average daily mean values of 8 W/m^2 in Toulouse, France, modulated by a diurnal cycle	Simulated AHF closer to inventory-based estimation	Bueno et al. (2011); Khalifa et al. (2016, 2018)
Bohnenstengel et al. (2014)	MORUSES	Meso	Top-down estimation	Annual average daily mean values of 2 W/m^2 in London, UK, modulated by a diurnal cycle	Smaller than the contribution of building-related AHF	None
Chow et al. (2014)	WRF-BEM+BEP	Meso	Bottom-up estimation	Diurnal varying (∼6–10 W/m^2) in Phoenix, US	Significance in quantifying AHF	F. Chen et al. (2016); B. Liu et al. (2021)
Juruš et al. (2016)	PALM-USM	Local	Bottom-up estimation	Diurnal varying (∼1–20 W/m^2) in Prague, Czech Republic	Insignificant changes in temperature and heat flux due to moderate traffic	Resler et al. (2017)

[1] Climate scale classification is: 10–200 m (micro), 0.5–2 km (local), and 25–100 km (meso) (Oke et al., 2017).

B2 Online Traffic Heat Modeling Using a Bottom-up Approach

We developed the urban traffic module that adopts the bottom-up method, involving both constant and time-varying parameters (Table B2).

Table B2. List of Traffic-Related Parameters.

Category	Parameter name	Unit	Long name	Reference & Data source
Morphological parameters (spatially varying)	N_{lane}	Unitless	Number of vehicle lanes	Model default surface data and Equation 4
	$Width_{\text{improad}}$	m	Impervious road width	Model default surface data and Equation 5
Climate-influenced parameters (with constant fundamental values)	$Speed$	m/s	Vehicle speed	Pigeon et al. (2008); World Health Organization (2018)
	E_{vehicle}	kW	Heat release into climate system per vehicle	Gasoline: Prusa et al. (2002); Diesel: Lee et al. (2017); Electric vehicle (EV): Ivanchev et al. (2020)
Traffic parameters (spatio-temporally varying)	AADT	vehicles/day-lane	Annual average daily traffic volume	Loder et al. (2019)
	p_v	Unitless (0–1)	Fraction of vehicle types	European Automotive Manufacturers Association (2024); International Energy Agency (IEA) (2024)

Based on Equation 4 and 5, the number of vehicle lanes (N_{lane}) shows limited spatial variability across global regions based in Jackson et al. (2010) data (Figure B1(a)–(c)). Tall building districts (TBD) typically have N_{lane} values in only a limited number of grid cells across East Asia, the USA, and select other regions (Figure B1(a)). High-density (HD) areas exhibit N_{lane} values of 1, 2, and 4 (Figure B1(b)). Most medium-density (MD) areas have only 1 and 2 vehicle lanes, and some regions in South Africa and South Asia do not have lanes (Figure B1(c)). In contrast, N_{lane} generated from the U-Surf, a 1 km urban parameter dataset, varies continuously across grid cells containing urban fractions (Figure B1(d)).

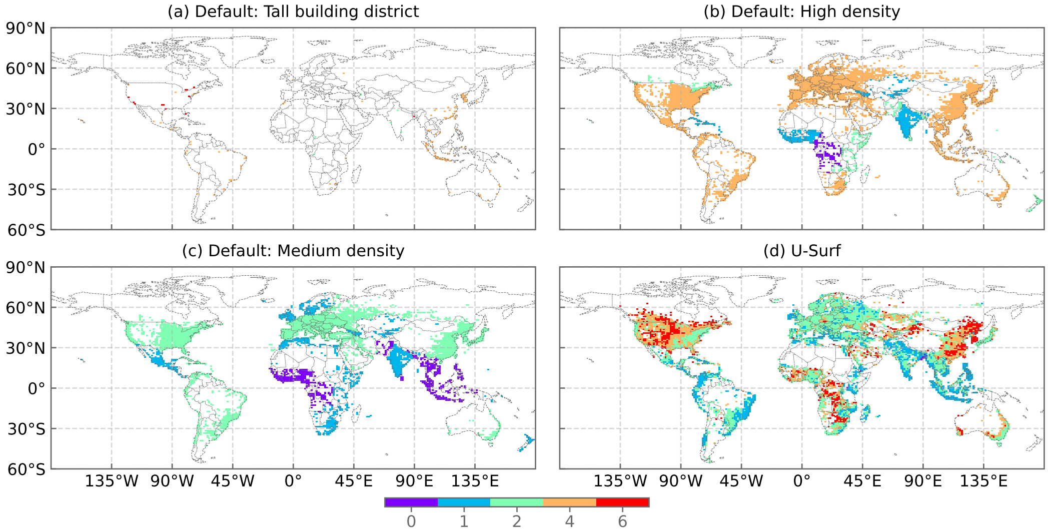

Figure B1. Number of vehicle lanes (N_{lane}). (a) Tall building district (TBD), (b) High density (HD), (c) Medium density (MD). Panels (a)–(c) show values from the default surface data at a grid spacing of 0.9° latitude and 1.25° longitude, with spatial variability across 33 global regions (Jackson et al., 2010). Panel (d) shows corresponding values from the U-Surf 1 km urban parameter dataset, with values continuously varying across grid cells (Cheng et al., 2025).

Appendix C Simulations

C1 Community Land Model-Urban (CLMU)

Community Terrestrial Systems Model (CTSM) takes a sub-grid approach to represent land cover types (Figure C1(a)). The CLMU is driven by atmospheric forcing at a certain reference height (Figure C1(b)). It has a building energy model, whose building space heating and waste heat sensible heat flux is moved to the canyon floor (i.e., pervious floor and impervious floor) (Figure C1(c)). Traffic-related sensible heat flux is added to the canyon floor rather than to the canopy air (Figure C1(d)).

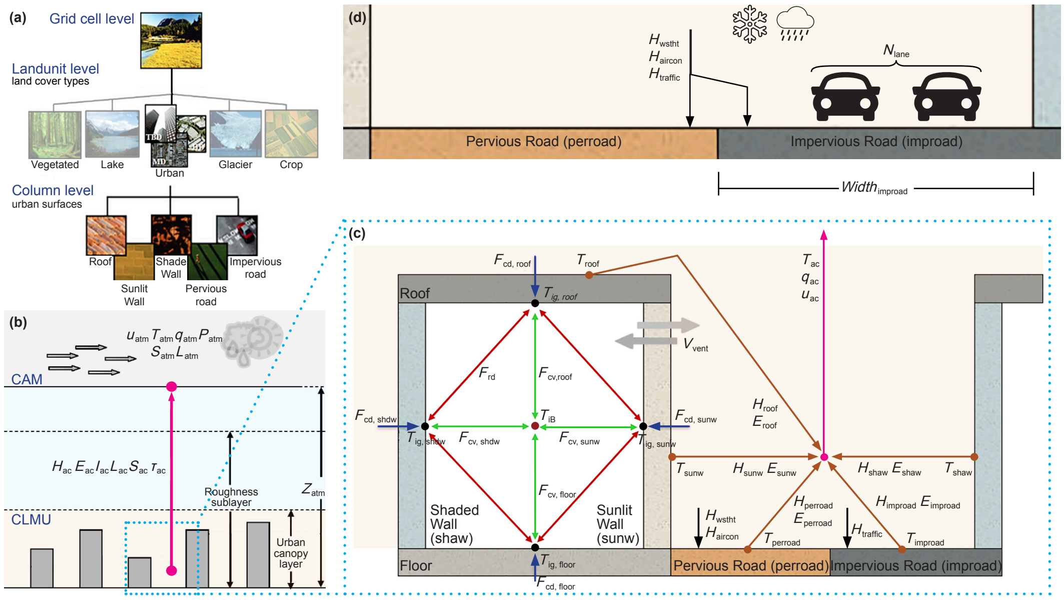

Figure C1. Community Land Model (CLM). (a) CLM representation hierarchy. (b) Interaction between the Community Atmosphere Model (CAM) and Community Land Model-Urban (CLMU). (c) Parameterization of CLMU. (d) Urban traffic modeling. Subplot (a)–(c) were modified based on Y. Sun et al. (2024).

C2 Input Data

CLMU represents FR-Capitole and UK-Manchester using their respective morphological, radiative, and thermal parameters (Table C1).

Table C1. Urban Parameters.

Parameter name	Long name	Unit	FR-Capitole	UK-Manchester
`CANYON_HWR`	Canyon height-to-width ratio	Unitless	1.32	0.75
`HT_ROOF`	Height of roof	meter	15	26
`NLEV_IMPROAD`	Number of impervious road layers	Unitless	2	
`THICK_ROOF`	Thickness of roof	meter	0.14	0.15
`THICK_WALL`	Thickness of wall	meter	0.29	
`WIND_HGT_CANYON`	Height of wind in canyon	meter	7.5	13
`WTLUNIT_ROOF`	Fraction of roof	Unitless	0.62	0.35
`WTROAD_PERV`	Fraction of pervious road out of total canyon floor	Unitless	0.26	0.69
`ALB_IMPROAD_DIF/` `ALB_IMPROAD_DIR`	Diffuse/direct albedo of impervious road	Unitless	0.13	
`ALB_PERROAD_DIF/` `ALB_PERROAD_DIR`	Diffuse/direct albedo of pervious road	Unitless	0.13	0.08
`ALB_ROOF_DIF/` `ALB_ROOF_DIR`	Diffuse/direct albedo of roof	Unitless	0.18	0.23
`ALB_WALL_DIF/` `ALB_WALL_DIR`	Diffuse/direct albedo of wall	Unitless	0.23	0.27
`EM_IMPROAD`	Emissivity of impervious road	Unitless	0.97	0.91
`EM_PERROAD`	Emissivity of pervious road	Unitless	0.99	0.94
`EM_ROOF`	Emissivity of roof	Unitless	0.92	0.89
`CV_IMPROAD`	Volumetric heat capacity of impervious road	kJ/ m^3 K	[2060.5, 1712.3]	
`CV_ROOF`	Volumetric heat capacity of roof	kJ/m^3 K	[1957.2, 994, 994, 1.2, 1.2, 1.2, 10.08, 10.08, 10.08, 609]	[1700, 1.2, 994, 1.2, 1.2, 1.2, 10.08, 10.08, 10.08, 609]
`CV_WALL`	Volumetric heat capacity of wall	kJ/m^3 K	[1524, 1525, 166, 918, 772, 771, 772, 227, 204, 628]	[1521, 1521, 138, 919, 773, 773, 773, 226, 194, 621]
`TK_IMPROAD`	Thermal conductivity of impervious road	W/m K	[1.67, 0.56]	
`TK_ROOF`	Thermal conductivity of roof	W/m K	[1.15, 0.15, 0.15, 0.03, 0.03, 0.03, 0.04, 0.04, 0.04, 0.16]	[1.2, 0.03, 0.15, 0.03, 0.03, 0.03, 0.04, 0.04, 0.04, 0.16]
`TK_WALL`	Thermal conductivity of wall	W/m K	[2.03, 6.15, 5.85, 6.21, 4.77, 0.66, 4.77, 5.7, 5.85, 1.81]	[2.52, 2.52, 0.15, 2.11, 0.68, 0.68, 0.68, 1.6, 2.23, 2.3]

[1] At FR-Capitole, urban parameters are from Urban-PLUMBER's detailed experiment. Among them, emissivity parameters are derived from CLM5.0's default dataset. That is, `EM_IMPROAD`, `EM_PERROAD`, and `EM_ROOF` were 0.97, 0.99, and 0.92, respectively. In the new dataset used for the CTSM development version, these values have been updated to 0.91, 0.95, and 0.91.

C3 Anthropogenic Heat Flux

Incorporating traffic heat emissions improves the comparability between the simulated AHF and the established AHF datasets (Table C2).

Table C2. List of Annual Mean Anthropogenic Heat Flux (AHF, unit: W/m^2).

Site name	FR-Capitole	UK-Manchester
CNTL simulation	6.25 for 2004	9.99 for 2022
TRAF simulation	27.72 for 2004	25.86 for 2022
AH4GUC for the 2010s (Varquez et al., 2021)	41.78	21.4
Jin et al. (2019)'s global gridded dataset for 2015	19.6	29.9
AH-DMSP for 2010 (Yang et al., 2017)	0.1	0.6

C4 Computational Cost

We evaluated the computational cost of the CNTL and TRAF simulations based on serial executions using a single CPU in ARCHER2. To minimize the influence of variability in CPU performance, each simulation was repeated five times, and the average timing values were used. The simulation timing consists of three stages: initialization, running, and finalization. Compared with the time for initialization and running, the finalization time is negligible. The running time is accumulated across model components, including the atmosphere, land, and coupler.

The urban traffic module affects both the model initialization and running processes (Figure C2(a)). In the TRAF simulation at the UK-Manchester site, the initialization time increases by 12.7 seconds, representing a 4.0% increase compared to the CNTL simulation. This is likely due to reading traffic input as well as calculating the number of vehicle lanes (N_{lane}) and impervious road width ($Width_{\mathrm{improad}}$). At the running stage, the FR-Capitole and UK-Manchester sites show increases of 1.2% and 2.7%, respectively. The land component accounts for the majority of the increase in computational cost (Figure C2(b)). The FR-Capitole and UK-Manchester sites showed increases of 2.4% and 5.9% in the land component (i.e., CTSM), respectively, while the atmosphere and coupler components exhibit only minor changes. Given that the simulations were conducted on a single CPU, the overall increase in computational cost remains relatively moderate.

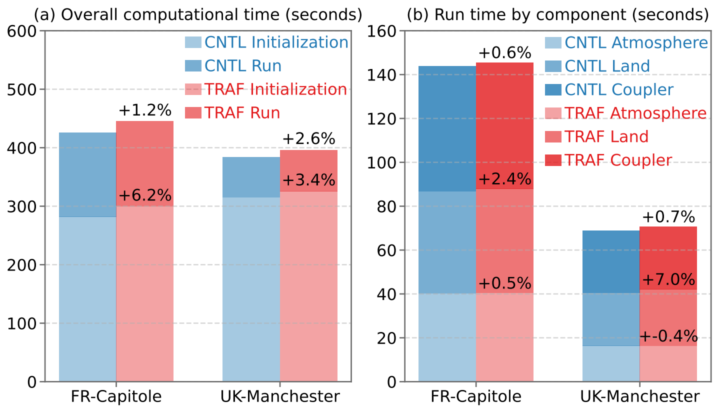

Figure C2. Timing comparison between CNTL and TRAF simulations. (a) Initialization and running times. (b) Running time by component.

Open Research

Community Earth System Model (CESM) source code is open access: `https://github.com/ESCOMP/CESM` (last access: 29 November 2025). Community Terrestrial Systems Model (CTSM) source code is available at: `https://github.com/ESCOMP/CTSM` (CTSM Development Team, 2025). The CTSM default input data set is available at `https://svn-ccsm-inputdata.cgd.ucar.edu/trunk/inputdata/lnd/clm2` (last access: 29 November 2025). Urban-PLUMBER data is open access at (Lipson et al., 2022a, 2022b). HadUK-Grid (1 km) data is open access at (Met Office et al., 2025). Global 1 km anthropogenic heat flux dataset, AH4GUC, is available at (Varquez et al., 2020). U-Surf 1 km urban parameter data is available at (Cheng et al., 2024). The modified source code, simulation input, scripts for simulation and output analysis, and other supplementary materials are available in the author's GitHub repository (Y. Sun & Zheng, 2025).

Acknowledgments

This work was supported by the Natural Environment Research Council [grant number UKRI1294], and the UKRI Harmonised Impact Acceleration Account, funded via the Economic & Social Research Council [grant number ES/X004759/1] and Engineering & Physical Sciences Research Council [grant number EP/X525753/1]. This work used the ARCHER2 UK National Supercomputing Service (`https://www.archer2.ac.uk`) and JASMIN, the UK's collaborative data analysis environment (`https://www.jasmin.ac.uk`). We gratefully acknowledge the traffic flow data from Transport for Greater Manchester (TfGM)'s VivaCity video analytics sensors. We appreciate Dr. Xiaodan Xu from Lawrence Berkeley National Laboratory for her valuable insights. Z.Z. appreciates the support provided by the academic start-up funds from the Department of Earth and Environmental Sciences at The University of Manchester. Y.S. is supported by Z.Z.'s academic start-up funds. Contributions from K.W.O. are based upon work supported by the NSF National Center for Atmospheric Research, which is a major facility sponsored by the U.S. National Science Foundation under Cooperative Agreement No. 1852977. We gratefully thank three anonymous reviewers for their constructive comments that substantially improved the manuscript. The authors declare no conflict of interest.

References

Afshari, A., Schuch, F., & Marpu, P. (2018). Estimation of the traffic related anthropogenic heat release using BTEX measurements – a case study in Abu Dhabi. *Urban Climate*, *24*, 311–325. doi: 10.1016/j.uclim.2017.02.001

Ayartürk, H., Doruk, E., Durgun, İ., & Ekbiç, K. (2016). New heating system development working with waste heat for electric vehicles. *Transportation Research Procedia*, *14*, 1080–1086. doi: 10.1016/j.trpro.2016.05.178

Beck, H. E., McVicar, T. R., Vergopolan, N., Berg, A., Lutsko, N. J., Dufour, A., ... Miralles, D. G. (2023). High-resolution (1 km) Köppen-Geiger maps for 1901–2099 based on constrained CMIP6 projections. *Scientific Data*, *10*(1), 724. doi: 10.1038/s41597-023-02549-6

Billot, R., El Faouzi, N.-E., & De Vuyst, F. (2009). Multilevel assessment of the impact of rain on drivers' behavior: Standardized methodology and empirical analysis. *Transportation Research Record*, *2107*(1), 134–142. doi: 10.3141/2107-14

Block, A., Keuler, K., & Schaller, E. (2004). Impacts of anthropogenic heat on regional climate patterns. *Geophysical Research Letters*, *31*(12). doi: 10.1029/2004GL019852

Bohnenstengel, S. I., Hamilton, I., Davies, M., & Belcher, S. E. (2014). Impact of anthropogenic heat emissions on London's temperatures. *Quarterly Journal of the Royal Meteorological Society*, *140*(679), 687–698. doi: 10.1002/qj.2144

Bueno, B., Norford, L., Pigeon, G., & Britter, R. (2011). Combining a detailed building energy model with a physically-based urban canopy model. *Boundary-Layer Meteorology*, *140*(3), 471–489. doi: 10.1007/s10546-011-9620-6

Bueno, B., Pigeon, G., Norford, L. K., Zibouche, K., & Marchadier, C. (2012). Development and evaluation of a building energy model integrated in the TEB scheme. *Geoscientific Model Development*, *5*(2), 433–448. doi: 10.5194/gmd-5-433-2012

Buzan, J. R., Oleson, K. W., & Huber, M. (2015). Implementation and comparison of a suite of heat stress metrics within the Community Land Model version 4.5. *Geoscientific Model Development*, *8*(2), 151–170. doi: 10.5194/gmd-8-151-2015

Chapman, L., & Thornes, J. E. (2005). The influence of traffic on road surface temperatures: Implications for thermal mapping studies. *Meteorological Applications*, *12*(4), 371–380. doi: 10.1017/S1350482705001957

Chen, B., Dong, L., Shi, G., Li, L., & Chen, L. (2014). Anthropogenic heat release: Estimation of global distribution and possible climate effect. *Journal of the Meteorological Society of Japan*, *92A*, 157–165. doi: 10.2151/jmsj.2014-A10

Chen, F., Kusaka, H., Bornstein, R., Ching, J., Grimmond, S., Grossman-Clarke, S., … Zhang, C. (2011). The integrated WRF/urban modelling system: Development, evaluation, and applications to urban environmental problems. *International Journal of Climatology*, *31*(2), 273–288. doi: 10.1002/joc.2158

Chen, F., Yang, X., & Wu, J. (2016). Simulation of the urban climate in a Chinese megacity with spatially heterogeneous anthropogenic heat data. *Journal of Geophysical Research: Atmospheres*, *121*(10), 5193–5212. doi: 10.1002/2015JD024642

Chen, X., & Yang, J. (2022). Potential benefit of electric vehicles in counteracting future urban warming: A case study of Hong Kong. *Sustainable Cities and Society*, *87*, 104200. doi: 10.1016/j.scs.2022.104200

Cheng, Y., Zhao, L., Chakraborty, T., Oleson, K., Demuzere, M., Liu, X., … Li, X. (2024). U-Surf: A global 1km spatially continuous urban surface property dataset for kilometer-scale urban-resolving Earth system modeling (1.1) [Dataset]. *Zenodo*. doi: 10.5281/zenodo.14695837

Cheng, Y., Zhao, L., Chakraborty, T. C., Oleson, K. W., Demuzere, M., Liu, X., … Li, X. C. (2025). U-Surf: A global 1 km spatially continuous urban surface property dataset for kilometer-scale urban-resolving Earth system modeling. *Earth System Science Data*, *17*(5), 2147–2174. doi: 10.5194/essd-17-2147-2025

Chow, W. T. L., Salamanca, F., Georgescu, M., Mahalov, A., Milne, J. M., & Ruddell, B. L. (2014). A multi-method and multi-scale approach for estimating city-wide anthropogenic heat fluxes. *Atmospheric Environment*, *99*, 64–76. doi: 10.1016/j.atmosenv.2014.09.053

CTSM Development Team. (2024). ESCOMP/CTSM: Add LILAC (ctsm1.0.dev104) [Software]. *Zenodo*. doi: 10.5281/zenodo.11176758

CTSM Development Team. (2025). ESCOMP/CTSM: CTSM 5.3: New surface datasets, git-fleximod intro, Leung dust, explicit AC, Matrix-CN, FATES transient LU, time/history metadata changes (ctsm5.3.021). *Zenodo*. doi: 10.5281/zenodo.14768518

Demuzere, M., Kittner, J., Martilli, A., Mills, G., Moede, C., Stewart, I. D., … Bechtel, B. (2022). A global map of local climate zones to support earth system modelling and urban-scale environmental science. *Earth System Science Data*, *14*(8), 3835–3873. doi: 10.5194/essd-14-3835-2022

Dong, Y., Varquez, A. C. G., & Kanda, M. (2017). Global anthropogenic heat flux database with high spatial resolution. *Scientific Data*, *150*, 276–294. doi: 10.1016/j.atmosenv.2016.11.040

Donkers, A., Yang, D., & Viktorović, M. (2020). Influence of driving style, infrastructure, weather and traffic on electric vehicle performance. *Transportation*

Research Part D: Transport and Environment, *88*, 102569. doi: 10.1016/j.trd.2020.102569
European Automotive Manufacturers Association. (2021). *Vehicles in use, Europe 2021* (Tech. Rep.). European Automobile Manufacturers' Association (ACEA).
European Automotive Manufacturers Association. (2024). *Vehicles on European Roads 2024* (Tech. Rep.). European Automotive Manufacturers' Association.
Ferreira, M. J., de Oliveira, A. P., & Soares, J. (2011). Anthropogenic heat in the city of São Paulo, Brazil. *Theoretical and Applied Climatology*, *104*(1), 43–56. doi: 10.1007/s00704-010-0322-7
Fischer, E. M., Oleson, K. W., & Lawrence, D. M. (2012). Contrasting urban and rural heat stress responses to climate change. *Geophysical Research Letters*, *39*(3), L0370. doi: 10.1029/2011GL050576
Flanner, M. G. (2009). Integrating anthropogenic heat flux with global climate models. *Geophysical Research Letters*, *36*(2), L02801. doi: 10.1029/2008GL036465
Fujimoto, A., Saida, A., & Fukuhara, T. (2012). A new approach to modeling vehicle-induced heat and its thermal effects on road surface temperature. *Journal of Applied Meteorology and Climatology*, *51*(11), 1980-1993. doi: 10.1175/JAMC-D-11-0156.1
Gao, J., & O'Neill, B. C. (2020). Mapping global urban land for the 21st century with data-driven simulations and Shared Socioeconomic Pathways. *Nature Communications*, *11*(1), 2302. doi: 10.1038/s41467-020-15788-7
Goret, M., Masson, V., Schoetter, R., & Moine, M.-P. (2019). Inclusion of CO2 flux modelling in an urban canopy layer model and an evaluation over an old European city centre. *Atmospheric Environment: X*, *3*, 100042. doi: 10.1016/j.aeaoa.2019.100042
Gou, X., Li, Z., Lan, T., Lin, J., Li, Z., Zhao, B., … Zhang, X. (2025). TraffiDent: A dataset for understanding the interplay between traffic dynamics and incidents. In *The Thirty-ninth Annual Conference on Neural Information Processing Systems Datasets and Benchmarks Track.* Retrieved from `https://openreview.net/forum?id=sZvXXPqONQ`
Habib, K., Hansdóttir, S. T., & Habib, H. (2020). Critical metals for electromobility: Global demand scenarios for passenger vehicles, 2015–2050. *Resources, Conservation and Recycling*, *154*, 104603. doi: 10.1016/j.resconrec.2019.104603
Haklay, M., & Weber, P. (2008). OpenStreetMap: User-generated street maps. *IEEE Pervasive Computing*, *7*(4), 12–18. doi: 10.1109/MPRV.2008.80
Hertwig, D., Ng, M., Grimmond, S., Vidale, P. L., & McGuire, P. C. (2021). High-resolution global climate simulations: Representation of cities. *International Journal of Climatology*, *41*(5), 3266–3285. doi: 10.1002/joc.7018
Hollis, D., McCarthy, M. P., Kendon, M., Legg, T., & Simpson, I. (2019). HadUK-Grid—a new UK dataset of gridded climate observations. *Geoscience Data Journal*, *64*(2), 151–159. doi: 10.1002/gdj3.78
Holman, C., Harrison, R., & Querol, X. (2015). Review of the efficacy of low emission zones to improve urban air quality in European cities. *Atmospheric Environment*, *111*, 161–169. doi: 10.1016/j.atmosenv.2015.04.009
Husni, E., Prayoga, G. A., Tamba, J. D., Retnowati, Y., Fauzandi, F. I., Yusuf, R., & Yahya, B. N. (2022). Microclimate investigation of vehicular traffic on the urban heat island through IoT-based device. *Heliyon*, *8*(11), e11739. doi: 10.1016/j.heliyon.2022.e11739
Iamarino, M., Beevers, S., & Grimmond, S. (2012). High-resolution (space, time) anthropogenic heat emissions: London 1970–2025. *International Journal of Climatology*, *32*(11), 1754–1767. doi: 10.1002/joc.2390
International Energy Agency (IEA). (2024). *Global EV Outlook 2024* (Tech. Rep.). Paris: International Energy Agency (IEA). Retrieved from `https://www.iea.org/reports/global-ev-outlook-2024`

Ivanchev, J., Fonseca, J., & Knoll, A. (2020). Electrification and automation of road transport: Impact analysis of heat and carbon emissions for Singapore. In *2020 IEEE 23rd International Conference on Intelligent Transportation Systems (ITSC)* (pp. 1–8). doi: 10.1109/ITSC45102.2020.9294274

Jackson, T. L., Feddema, J. J., Oleson, K. W., Bonan, G. B., & Bauer, J. T. (2010). Parameterization of urban characteristics for global climate modelling. *Annals of the Association of American Geographers*, *100*(4), 848–865. doi: 10.1080/00045608.2010.497328

Jägerbrand, A. K., & Sjöbergh, J. (2016). Effects of weather conditions, light conditions, and road lighting on vehicle speed. *SpringerPlus*, *5*(1), 505. doi: 10.1186/s40064-016-2124-6

Jin, K., Wang, F., Chen, D., Liu, H., Ding, W., & Shi, S. (2019). A new global gridded anthropogenic heat flux dataset with high spatial resolution and long-term time series. *Scientific Data*, *6*(1), 139. doi: 10.1038/s41597-019-0143-1

Juruš, P., Resler, J., Derbek, P., Krč, P., Belda, M., Benešová, N., ... Hrubeš, P. (2016). High resolution modelling of anthropogenic heat from traffic in urban canopy: A sensitivity study. In *2016 Smart Cities Symposium Prague (SCSP)* (pp. 1–6). doi: 10.1109/SCSP.2016.7501031

Khalifa, A., Bouzouidja, R., Marchetti, M., Buès, M., Bouilloud, L., Martin, E., & Chancibaut, K. (2018). Individual contributions of anthropogenic physical processes associated to urban traffic in improving the road surface temperature forecast using TEB model. *Urban Climate*, *24*, 778–795. doi: 10.1016/j.uclim.2017.09.003

Khalifa, A., Marchetti, M., Bouilloud, L., Martin, E., Bues, M., & Chancibaut, K. (2016). Accounting for anthropic energy flux of traffic in winter urban road surface temperature simulations with the TEB model. *Geoscientific Model Development*, *9*(2), 547–565. doi: 10.5194/gmd-9-547-2016

Kikegawa, Y., Tanaka, A., Ohashi, Y., Ihara, T., & Shigeta, Y. (2014). Observed and simulated sensitivities of summertime urban surface air temperatures to anthropogenic heat in downtown areas of two Japanese Major Cities, Tokyo and Osaka. *Theoretical and Applied Climatology*, *117*(1), 175–193. doi: 10.1007/s00704-013-0996-8

Kim, Y., Yeo, H., & Kim, Y. (2022). Estimating urban spatial temperatures considering anthropogenic heat release factors focusing on the mobility characteristics. *Sustainable Cities and Society*, *85*, 104073. doi: 10.1016/j.scs.2022.104073

Lee, J., & Berkelhammer, M. (2025). Evaluating the influence of traffic congestion on surface urban heat island intensity. *Geophysical Research Letters*, *52*(16), e2025GL116651. doi: 10.1029/2025GL116651

Lee, J., Chu, S., Min, K., Kim, M., Jung, H., Kim, H., & Chi, Y. (2017). Classification of diesel and gasoline dual-fuel combustion modes by the analysis of heat release rate shapes in a compression ignition engine. *Fuel*, *209*, 587–597. doi: 10.1016/j.fuel.2017.07.067

Li, B., Yu, R., Chen, Z., Ding, Y., Yang, M., Li, J., ... Zhong, H. (2024). High-resolution multi-source traffic data in New Zealand. *Scientific Data*, *11*(1), 1216. doi: 10.1038/s41597-024-04067-5

Li, C., Zhang, N., Wang, Y., & Chen, Y. (2023). Modeling urban heat islands and thermal comfort during a heat wave event in East China with CLM5 incorporating local climate zones. *Journal of Geophysical Research: Atmospheres*, *128*(16), e2023JD038883. doi: 10.1029/2023JD038883

Li, X. C., Zhao, L., Oleson, K. W., Zhou, Y., Qin, Y., Zhang, K., & Fang, B. (2024). Enhancing urban climate-energy modeling in the Community Earth System Model (CESM) through explicit representation of urban air-conditioning adoption. *Journal of Advances in Modeling Earth Systems*, *16*(4), e2023MS004107. doi: 10.1029/2023MS004107

Liao, W., Li, Y., Liu, X., Wang, Y., Che, Y., Shao, L., … Chen, F. (2025). GloUCP: A global 1 km spatially continuous urban canopy parameters for the WRF model. *Earth System Science Data*, *17*(6), 2535–2551. doi: 10.5194/essd-17-2535-2025

Lipson, M. J., Grimmond, S., Best, M., Abramowitz, G., Coutts, A., Tapper, N., … Pitman, A. J. (2023). Evaluation of 30 urban land surface models in the Urban-PLUMBER project: Phase 1 results. *Quarterly Journal of the Royal Meteorological Society*, *150*(758), 126-169. doi: 10.1002/qj.4589

Lipson, M. J., Grimmond, S., Best, M., Chow, W., Christen, A., Chrysoulakis, N., … Ward, H. C. (2022a). Data for "Harmonized gap-filled dataset from 20 urban flux tower sites" for the Urban-PLUMBER project (v1) [Dataset]. *Zenodo*. doi: 10.5281/zenodo.5517550

Lipson, M. J., Grimmond, S., Best, M., Chow, W. T. L., Christen, A., Chrysoulakis, N., … Ward, H. C. (2022b). Harmonized gap-filled datasets from 20 urban flux tower sites. *Earth System Science Data*, *14*(11), 5157–5178. doi: 10.5194/essd-14-5157-2022

Liu, B., Xie, Z., Qin, P., Liu, S., Li, R., Wang, L., … Shi, C. (2021). Increases in anthropogenic heat release from energy consumption lead to more frequent extreme heat events in urban cities. *Advances in Atmospheric Sciences*, *38*(3), 430–445. doi: 10.1007/s00376-020-0139-y

Liu, C., S., Yusak O., & and Karlström, A. (2017). Weather variability and travel behaviour – what we know and what we do not know. *Transport Reviews*, *37*(6), 715–741. doi: 10.1080/01441647.2017.1293188

Loder, A., Ambühl, L., Menendez, M., & Axhausen, K. W. (2019). Understanding traffic capacity of urban networks. *Scientific Reports*, *9*(1), 16283. doi: 10.1038/s41598-019-51539-5

Manchester City Council. (2022). *Manchester electric vehicle charging strategy* (Tech. Rep.). Manchester: Manchester City Council. Retrieved from `https://democracy.manchester.gov.uk/documents/s41761/EV%20Update.pdf`

Masson, V., Gomes, L., Pigeon, G., Liousse, C., Pont, V., Lagouarde, J.-P., … Tulet, P. (2008). The Canopy and Aerosol Particles Interactions in TOulouse Urban Layer (CAPITOUL) experiment. *Meteorology and Atmospheric Physics*, *102*(3), 135–157. doi: 10.1007/s00703-008-0289-4

McCarthy, M. P., Armstrong, L., & Armstrong, N. (2019). A new heatwave definition for the UK. *Weather*, *74*(11), 382–387. doi: 10.1002/wea.3629

McCarthy, M. P., Best, M. J., & Betts, R. A. (2010). Climate change in cities due to global warming and urban effects. *Geophysical Research Letters*, *37*(9), L09705. doi: 10.1029/2010GL042845

McCarthy, M. P., Harpham, C., Goodess, C. M., Jones, P. D., Xian, G., Shi, H., … Kolian, M. (2012). Simulating climate change in UK cities using a regional climate model, HadRM3. *GIScience & Remote Sensing*, *32*(12), 1875–1888. doi: 10.1002/joc.2402

Met Office, Hollis, D., Carlisle, E., Kendon, M., Packman, S., & Doherty, A. (2025). HadUK-Grid gridded climate observations on a 1km grid over the UK, v1.3.1.ceda (1836-2024) [Dataset]. *NERC EDS Centre for Environmental Data Analysis*. doi: 10.5285/F02CC6DDD92F45B18B9AB6AB544DF7D9

Ming, Y., Liu, Y., & Liu, X. (2022). Spatial pattern of anthropogenic heat flux in monocentric and polycentric cities: The case of Chengdu and Chongqing. *Sustainable Cities and Society*, *78*, 103628. doi: 10.1016/j.scs.2021.103628

Mužić, I., Hodnebrog, Ø., Yilmaz, Y. A., Berntsen, T. K., Lawrence, D. M., & Sobhani, N. (2025). The evaluation of hydroclimatic variables over Nordic Fennoscandia using WRF-CTSM. *Journal of Geophysical Research: Atmospheres*, *130*(9), e2024JD043103. doi: 10.1029/2024JD043103

Neog, R., Acharjee, S., & Hazarika, J. (2021). Spatiotemporal analysis of road surface temperature (RST) and building wall temperature (BWT) and its relation to the traffic volume at Jorhat urban environment, India. *Environment, Development and Sustainability*, *23*(7), 10080–10092. doi: 10.1007/s10668-020-01047-8

Ohashi, Y., Genchi, Y., Kondo, H., Kikegawa, Y., Yoshikado, H., & Hirano, Y. (2007). Influence of air-conditioning waste heat on air temperature in Tokyo during summer: Numerical experiments using an urban canopy model coupled with a building energy model. *Journal of Applied Meteorology and Climatology*, *46*, 66–81. doi: 10.1175/JAM2441.1

Oke, T. R., Mills, G., Christen, A., & Voogt, J. A. (2017). *Urban climates.* Cambridge University Press.

Oleson, K. W., Bonan, G. B., Feddema, J. J., Vertenstein, M., & Grimmond, C. S. B. (2008). An urban parameterization for a global climate model. Part I: Formulation and evaluation for two cities. *Journal of Applied Meteorology and Climatology*, *47*(4), 1038–1060. doi: 10.1175/2007JAMC1597.1

Oleson, K. W., Bonan, G. B., Feddema, J. J., Vertenstein, M., & Kluzek, E. (2010). *Technical description of an urban parameterization for the Community Land Model (CLMU)* (Tech. Rep.). Boulder, Colorado, USA: University Corporation for Atmospheric Research.

Oleson, K. W., & Feddema, J. J. (2020). Parameterization and surface data improvements and new capabilities for the Community Land Model Urban (CLMU). *Journal of Advances in Modeling Earth Systems*, *12*(2), e2018MS001586. doi: 10.1029/2018MS001586

Padget, E. D., Knapp, K. K., & Thomas, G. B. (2001). Investigation of winter-weather speed variability in sport utility vehicles, pickup trucks, and passenger cars. *Transportation Research Record*, *1779*(1), 116–124. doi: 10.3141/1779-16

Pesaresi, M., & Politis, P. (2023). GHS-BUILT-H R2022A - GHS building height, derived from AW3D30, SRTM30, and Sentinel2 composite (2018) [Dataset]. *European Commission, Joint Research Centre (JRC).* doi: 10.2905/85005901-3A49-48DD-9D19-6261354F56FE

Pigeon, G., Legain, D., Durand, P., & Masson, V. (2007). Anthropogenic heat release in an old European agglomeration (Toulouse, France). *International Journal of Climatology*, *27*(14), 1969–1981. doi: 10.1002/joc.1530

Pigeon, G., Moscicki, M. A., Voogt, J. A., & Masson, V. (2008). Simulation of fall and winter surface energy balance over a dense urban area using the TEB scheme. *Meteorology and Atmospheric Physics*, *102*(3), 159–171. doi: 10.1007/s00703-008-0320-9

Pokorný, P. (2017). Determining traffic levels in cities using Google Maps. In *2017 Fourth International Conference on Mathematics and Computers in Sciences and in Industry (MCSI)* (pp. 144–147). doi: 10.1109/MCSI.2017.33

Prusa, J. M., Segal, M., Temeyer, B. R., Gallus, W. A., & Takle, E. S. (2002). Conceptual and scaling evaluation of vehicle traffic thermal effects on snow/ice-covered roads. *Journal of Applied Meteorology and Climatology*, *41*(12), 1225-1240. doi: 10.1175/1520-0450(2002)041⟨1225:CASEOV⟩2.0.CO;2

Rakha, H., Arafeh, M., & Park, S. (2012). Modeling inclement weather impacts on traffic stream behavior. *International Journal of Transportation Science and Technology*, *1*(1), 25–47. doi: 10.1260/2046-0430.1.1.25

Resler, J., Krč, P., Belda, M., Juruš, P., Benešová, N., Lopata, J., … Kanani-Sühring, F. (2017). PALM-USM v1.0: A new urban surface model integrated into the PALM large-eddy simulation model. *Geoscientific Model Development*, *10*(10), 3635–3659. doi: 10.5194/gmd-10-3635-2017

Righi, M., Hendricks, J., & Brinkop, S. (2023). The global impact of the transport sectors on the atmospheric aerosol and the resulting climate effects under the Shared Socioeconomic Pathways (SSPs). *Earth System Dynamics*, *14*(4), 835–859. doi: 10.5194/esd-14-835-2023

Ryu, Y.-H., & Min, S.-K. (2024). Anthropogenic warming degrades spring air quality in Northeast Asia by enhancing atmospheric stability and transboundary transport. *npj Climate and Atmospheric Science*, *7*(1), 1–10. doi: 10.1038/s41612-024-00603-7

Sailor, D. J., Georgescu, M., Milne, J. M., & Hart, M. A. (2015). Development of a national anthropogenic heating database with an extrapolation for international cities. *Atmospheric Environment*, *118*, 7–18. doi: 10.1016/j.atmosenv.2015.07.016

Sailor, D. J., & Lu, L. (2004). A top–down methodology for developing diurnal and seasonal anthropogenic heating profiles for urban areas. *Atmospheric Environment*, *38*(17), 2737–2748. doi: 10.1016/j.atmosenv.2004.01.034

Shahmohamadi, P., Che-Ani, A. I., Maulud, K. N. A., Tawil, N. M., & Abdullah, N. A. G. (2011). The impact of anthropogenic heat on formation of urban heat island and energy consumption balance. *Urban Studies Research*, *2011*(1), 497524. doi: 10.1155/2011/497524

Shui, B., Shafique, M., & Luo, X. (2024). Light-duty passenger vehicle electrification in China from 2021 to 2050 and associated greenhouse gas emissions: A dynamic fleet perspective. *Transportation Research Part D: Transport and Environment*, *130*, 104199. doi: 10.1016/j.trd.2024.104199

Skuza, A., & Jurecki, R. S. (2022). Analysis of factors affecting the energy consumption of an EV vehicle - a literature study. *IOP Conference Series: Materials Science and Engineering*, *1247*(1), 012001. doi: 10.1088/1757-899X/1247/1/012001

Smith, C., Lindley, S., & Levermore, G. (2009). Estimating spatial and temporal patterns of urban anthropogenic heat fluxes for UK cities: The case of Manchester. *Theoretical and Applied Climatology*, *98*(1), 19–35. doi: 10.1007/s00704-008-0086-5

Sun, R., Wang, Y., & Chen, L. (2018). A distributed model for quantifying temporal-spatial patterns of anthropogenic heat based on energy consumption. *Journal of Cleaner Production*, *170*, 601–609. doi: 10.1016/j.jclepro.2017.09.153

Sun, Y., Fang, B., Oleson, K. W., Zhao, L., Topping, D. O., Schultz, D. M., & Zheng, Z. (2024). Improving urban climate adaptation modelling in the Community Earth System Model (CESM) through transient urban surface albedo representation. *Journal of Advances in Modeling Earth Systems*, *16*(12), e2024MS004380. doi: 10.1029/2024MS004380

Sun, Y., Oleson, K. W., Zhao, L., Mills, G., He, C., Demuzere, M., … Zheng, Z. (2025). Enhancing global-scale urban land cover representation using local climate zones in the Community Earth System Model. *Journal of Advances in Modeling Earth Systems*, *17*(11), e2025MS004934. doi: 10.1029/2025MS004934

Sun, Y., & Zheng, Z. (2025). envdes/code_CLMU_traffic: First release (v0.0.0) [Software]. *Zenodo*. doi: 10.5281/zenodo.16886810

Takane, Y., Nakajima, K., & Kikegawa, Y. (2022). Urban climate changes during the COVID-19 pandemic: Integration of urban-building-energy model with social big data. *npj Climate and Atmospheric Science*, *5*(1), 1–10. doi: 10.1038/s41612-022-00268-0

Tanimura, R., Hiromori, A., Umedu, T., Yamaguchi, H., & Higashino, T. (2015). Prediction of deceleration amount of vehicle speed in snowy urban roads using weather information and traffic data. In *2015 IEEE 18th International Conference on Intelligent Transportation Systems* (pp. 2268–2273). doi: 10.1109/ITSC.2015.366

Tao, H., Xing, J., Pan, G., Pleim, J., Ran, L., Wang, S., … Li, J. (2021). Impact of anthropogenic heat emissions on meteorological parameters and air quality in Beijing using a high-resolution model simulation. *Frontiers of Environmental*

Science & Engineering, *16*(4), 44. doi: 10.1007/s11783-021-1478-3
Taylor, K. E. (2001). Summarizing multiple aspects of model performance in a single diagram. *Journal of Geophysical Research: Atmospheres*, *106*(D7), 7183–7192. doi: 10.1029/2000JD900719
Teufel, B., Sushama, L., Poitras, V., Dukhan, T., Bélair, S., Miranda-Moreno, L., ... Bitsuamlak, G. (2021). Impact of COVID-19-related traffic slowdown on urban heat characteristics. *Atmosphere*, *12*(2), 243. doi: 10.3390/atmos12020243
Thomas, C. E. (2009). Fuel cell and battery electric vehicles compared. *International Journal of Hydrogen Energy*, *34*(15), 6005–6020. doi: 10.1016/j.ijhydene.2009.06.003
van Strien, M. J., & Grêt-Regamey, A. (2024). A global time series of traffic volumes on extra-urban roads. *Scientific Data*, *11*(1), 470. doi: 10.1038/s41597-024-03287-z
Varquez, A. C. G., Kiyomoto, S., Khanh, D. N., & Kanda, M. (2020). Global 1-km present and future hourly anthropogenic heat flux (v6) [Dataset]. *figshare*. doi: 10.6084/m9.figshare.12612458.v6
Varquez, A. C. G., Kiyomoto, S., Khanh, D. N., & Kanda, M. (2021). Global 1-km present and future hourly anthropogenic heat flux. *Scientific Data*, *8*(1), 64. doi: 10.1038/s41597-021-00850-w
Wang, L., Li, D., & Yuan, X. (2025). The role of vapor pressure deficit in the CLM simulated interaction between urban heat islands and heat waves over conus. *Geophysical Research Letters*, *52*(6), e2024GL113257. doi: 10.1029/2024GL113257
Washington, W. M. (1972). Numerical climatic-change experiments: The effect of man's production of thermal energy. *Journal of Applied Meteorology (1962-1982)*, *11*(5), 768–772.
World Health Organization. (2018). *Global status report on road safety 2018* (Tech. Rep.). Geneva: World Health Organization.
Xia, J., Ling, F., Li, Z. J., Yu, J., Zhang, H., Topping, D., ... Zheng, Z. (2025). Learning urban climate dynamics via physics-guided urban surface–atmosphere interactions. In *The Thirty-ninth Annual Conference on Neural Information Processing Systems.* Retrieved from `https://openreview.net/forum?id=i9BjNoVjub`
Xiao, S., Neti, S., Suleiman, M. T., & Naito, C. (2018). A modeling approach of heat transfer of bridges considering vehicle-induced thermal effects. *Journal of Applied Meteorology and Climatology*, *57*(12), 2851–2869. doi: 10.1175/JAMC-D-17-0315.1
Xie, M., Liao, J., Wang, T., Zhu, K., Zhuang, B., Han, Y., ... Li, S. (2016). Modeling of the anthropogenic heat flux and its effect on regional meteorology and air quality over the Yangtze River Delta region, China. *Atmospheric Chemistry and Physics*, *16*(10), 6071–6089. doi: 10.5194/acp-16-6071-2016
Xie, Y., Li, Y., Zhao, Z., Dong, H., Wang, S., Liu, J., ... Duan, X. (2020). Microsimulation of electric vehicle energy consumption and driving range. *Applied Energy*, *267*, 115081. doi: 10.1016/j.apenergy.2020.115081
Xu, X., Zheng, Z., Hu, Z., Feng, K., & Ma, W. (2024). A unified dataset for the city-scale traffic assignment model in 20 U.S. cities. *Scientific Data*, *11*(1), 325. doi: 10.1038/s41597-024-03149-8
Yan, L., Zhang, Q., Zheng, B., & He, K. (2024). Modeling fuel-, vehicle-type-, and age-specific CO_2 emissions from global on-road vehicles in 1970–2020. *Earth System Science Data*, *16*(10), 4497–4509. doi: 10.5194/essd-16-4497-2024
Yang, W., Luan, Y., Liu, X., Yu, X., Miao, L., & Cui, X. (2017). A new global anthropogenic heat estimation based on high-resolution nighttime light data. *Scientific Data*, *4*(1), 170116. doi: 10.1038/sdata.2017.116
Yu, J., Sun, Y., Lindley, S., Jay, C., Topping, D. O., Oleson, K. W., & Zheng, Z. (2025). Integration and execution of Community Land Model Urban (CLMU)

in a containerized environment. *Environmental Modelling & Software*, *188*, 106391. doi: 10.1016/j.envsoft.2025.106391

Yu, J., Zheng, Z., Lindley, S., Zhao, L., Wang, C., Wu, Q., … Oleson, K. W. (2025). Leveraging Automated Machine Learning (AutoML) for Urban Climate Emulation. *Big Data and Earth System*, 100040. doi: 10.1016/j.bdes.2025.100040

Zhang, G. J., Cai, M., & Hu, A. (2013). Energy consumption and the unexplained winter warming over northern Asia and North America. *Nature Climate Change*, *3*(5), 466–470. doi: 10.1038/nclimate1803

Zhang, K., Fang, B., Oleson, K., Zhao, L., He, C., Huang, Q., … Lee, X. (2025). Urban land expansion amplifies surface warming more in dry climate than in wet climate: A global sensitivity study. *Journal of Geophysical Research: Atmospheres*, *130*(4), e2024JD041696. doi: 10.1029/2024JD041696

Zhang, L., Yan, Z., Huang, K., & Zhang, W. (2025). Evaluation and statistical bias correction of ERA5-Land meteorological variables for a humid river basin in Southwest China. *Scientific Reports*, *15*(1), 41101. doi: 10.1038/s41598-025-24942-4

Zhang, N., Wang, X., Chen, Y., Dai, W., & Wang, X. (2010). Numerical simulations on influence of urban land cover expansion and anthropogenic heat release on urban meteorological environment in Pearl River Delta. *Building Services Engineering Research and Technology*, *126*(3-4), 398–403. doi: 10.1007/s00704-015-1601-0

Zhang, R., & Fujimori, S. (2020). The role of transport electrification in global climate change mitigation scenarios. *Environmental Research Letters*, *15*(3), 034019. doi: 10.1088/1748-9326/ab6658

Zhao, L., Oleson, K., Bou-Zeid, E., Krayenhoff, E. S., Bray, A., Zhu, Q., … Oppenheimer, M. (2021). Global multi-model projections of local urban climates. *Nature Climate Change*, *11*(2), 152–157. doi: 10.1038/s41558-020-00958-8

Zheng, Z., Zhao, L., & Oleson, K. W. (2021). Large model structural uncertainty in global projections of urban heat waves. *Nature Communications*, *12*(1), 3736. doi: 10.1038/s41467-021-24113-9